A Full Eulerian Fluid-Membrane Coupling Method with a Smoothed Volume-of-Fluid Approach

Satoshi Ii[1,*], Xiaobo Gong[2], Kazuyasu Sugiyama[1], Jinbiao Wu[3], Huaxiong Huang[4] and Shu Takagi[1,5]

[1] *Department of Mechanical Engineering, The University of Tokyo, 7-3-1 Hongo Bunkyo-ku, Tokyo, 113-8656, Japan.*
[2] *Department of Engineering Mechanics, NAOCE, Shanghai Jiaotong University, Shanghai 200240, China.*
[3] *LMAM & School of Mathematical Sciences, Peking University, Beijing 100871, China.*
[4] *Department of Mathematics and Statistics, York University, 4700 Keele Street, Toronto, Ontario, Canada.*
[5] *Computational Science Research Program, RIKEN, 2-1 Hirosawa Wako, Saitama, 351-0198, Japan.*

Abstract. A novel full Eulerian fluid-elastic membrane coupling method on the fixed Cartesian coordinate mesh is proposed within the framework of the volume-of-fluid approach. The present method is based on a full Eulerian fluid-(bulk) structure coupling solver (Sugiyama *et al.*, *J. Comput. Phys.*, **230** (2011) 596–627), with the bulk structure replaced by elastic membranes. In this study, a closed membrane is considered, and it is described by a volume-of-fluid or volume-fraction information generally called VOF function. A smoothed indicator (or characteristic) function is introduced as a phase indicator which results in a smoothed VOF function. This smoothed VOF function uses a smoothed delta function, and it enables a membrane singular force to be incorporated into a mixture momentum equation. In order to deal with a membrane deformation on the Eulerian mesh, a deformation tensor is introduced and updated within a compactly supported region near the interface. Both the neo-Hookean and the Skalak models are employed in the numerical simulations. A smoothed (and less dissipative) interface capturing method is employed for the advection of the VOF function and the quantities defined on the membrane. The stability restriction due to membrane stiffness is relaxed by using a quasi-implicit approach. The present method is validated by using the spherical membrane deformation problems, and is applied to a pressure-driven flow with the biconcave membrane capsules (red blood cells).

Corresponding author. Email addresses: `sii@fel.t.u-tokyo.ac.jp` (S. Ii), `x.gong@sjtu.edu.cn` (X. Gong), `sugiyama@fel.t.u-tokyo.ac.jp` (K. Sugiyama), `jwu@math.pku.edu.cn` (J. Wu), `hhuang@yorku.ca` (H. Huang), `takagi@mech.t.u-tokyo.ac.jp` (S. Takagi)

1 Introduction

To compute the solutions of fluid-membrane interaction problems where the motion of the fluid is coupled with the motion and deformation of embedded membranes, efficient numerical methods that can be implemented easily are often required. The immersed boundary method developed by Peskin [40, 41] is one of the most successful for these types of problems. Under the framework of the immersed boundary method, the fluid equations are solved in an Eulerian frame, while the elastic membrane is tracked in a Lagrangian manner by a set of marker points. The force exerted by the membrane on the Eulerian flow field is interpolated with the smoothed (or approximate) delta function. The immersed boundary method has been applied to a wide variety of biological problems [10, 12, 14, 15]. Many refinements and extensions have been proposed over the past several decades. For example, a new version of the method was proposed in [29] that achieves the second-order accuracy for problems with smooth solutions. The front tracking method [18, 51, 52] can be applied to multi-phase flow problems including the surface tension effect with different fluid properties. Moreover, the immersed interface method [30, 31, 33] provides a recipe for developing schemes for problems with piecewise smooth solutions, by introducing the modified Taylor expansion with the interfacial jump conditions. In these schemes, the interface can be accurately represented by the Lagrangian particles, which is of particular interests when the interface has structures that are under the resolution of the fixed Eulerian mesh. On the other hand, the particle-based methods do not automatically conserve the volume or mass encompassed by the surface reconstructed from the marker particles, and the largely distorted surface meshes may lead to a numerical instability.

In order to overcome such problems, full Eulerian approaches were proposed for the fluid-structure interaction [4, 7, 9, 25, 34, 37, 38, 48, 49, 53, 54] and fluid-membrane interaction [6]. Rather than using the Lagrangian particles, field variables or functions to identify the interface are defined and updated on the Eulerian mesh. Cottet *et al.* [6] introduced the level-set function to identify the interface, in addition, the membrane stretching or variation of the surface area was obtained from the information of the level-set function. As a result, the membrane force was successfully obtained on the Eulerian mesh without using the interfacial material points. However, since the constitutive law of the membrane elasticity is limited to a model which only involves a variation of the surface area, it has not been applied yet for more general membrane models which depend on the principal strains. Recently, Sugiyama *et al.* [49] formulated a fluid-structure interaction model based on the full Eulerian framework for an incompressible fluid and

hyperelastic bulk solid, and this model was applied to a pressure-induced flow with biconcave elastic particles [48] and a hyperelastic wavy channel [37]. The basic ideas are to describe each phase (fluid or solid) with the solid/fluid volume-fraction data, so-called volume-of-fluid (VOF) function [23], and a left Cauchy-Green deformation tensor to represent the solid deformation. The method is applicable to general hyperelastic materials immersed in an incompressible viscous fluid.

In the present paper, we propose a novel full Eulerian fluid-membrane interaction method, as an extension of the general ideas in Sugiyama *et al.* [49]. The main difference between the current work and that reported in [49] lies in the immersed elastic materials. The immersed membrane is represented by a smoothly-defined VOF function on the Eulerian mesh, and an approximate delta function given from the smoothed VOF function enables a membrane singular force to be incorporated into a mixture momentum equation. In order to deal with the membrane deformation on the Eulerian mesh, a part of the surface left Cauchy-Green deformation tensor is introduced and updated. The introduced surface deformation tensor enables to take account of the neo-Hookean model and Skalak model which is generally used in a practical model of a red blood cell. From a numerical point of view, a continuous (less dissipative) interface capturing method, namely MTHINC method [24, 26] developed from [55, 56], is employed for the advection of the VOF function. Moreover, a convolution technique is newly proposed with coupling with the MTHINC method for the advection of a quantity defined on the membrane to suppress the numerical dissipation. In addition, we extend the quasi-implicit formulation [25] to the membrane stress treatment to relax a numerical stability restriction caused by membrane stiffness.

This rest of the paper is organized as follows. The numerical approach including the membrane model, basic equations and discretization, is described in Section 2. The validations in the advection and interaction problems, and the extension to a flow including the biconcave capsules are shown in Section 3. Finally, we conclude this paper with some remarks in Section 4.

2   Mathematical formulation and numerical method

2.1   Membrane model

We follow the basic derivation of the large deformable membrane model [1, 45]. The deformation gradient tensor $\mathbf{F}$ is defined as $\mathbf{F} = \partial \mathbf{x} / \partial \mathbf{X}$, where $\mathbf{x}$ is a current coordinate and $\mathbf{X}$ is a reference coordinate in a stretch-free condition. Since the thickness of the membrane is often negligible comparing to its size, in the present approach based on continuum mechanics, the relationships $\mathbf{n} \cdot \mathbf{F}_s = \mathbf{0}$ and $\mathbf{F}_s \cdot \mathbf{n}_R = \mathbf{0}$ for the surface deformation gradient tensor should be satisfied. Here $\mathbf{n}$ and $\mathbf{n}_R$ are the unit normal vectors in a current configuration and reference configuration, respectively. Therefore, the surface deformation gradient tensor $\mathbf{F}_s$ is given by

$$\mathbf{F}_s = \mathbf{P} \cdot \mathbf{F} \cdot \mathbf{P}_R, \tag{2.1}$$

where $\mathbf{P} = \mathbf{I} - \mathbf{nn}$ and $\mathbf{P}_R = \mathbf{I} - \mathbf{n}_R\mathbf{n}_R$ are the surface projection tensors. Then the surface left Cauchy-Green deformation tensor $\mathbf{B}_s$ is defined as

$$\mathbf{B}_s = \mathbf{F}_s \cdot \mathbf{F}_s^T. \tag{2.2}$$

For hyperelastic membranes, it is convenient to use surface strain energy function W_s, which consists of the surface invariants $I_{1,2}$ of the surface left Cauchy-Green deformation tensor. The surface invariants $I_{1,2}$ can be expressed as

$$I_1 = \text{tr}(\mathbf{B}_s) - 2 \quad \text{and} \quad I_2 = \left(\text{tr}(\mathbf{B}_s)^2 - \text{tr}(\mathbf{B}_s^2)\right)/2 - 1.$$

In this paper, they are rewritten as

$$c_1 = I_1 + 1 = \text{tr}(\mathbf{B}_s) - 1, \tag{2.3a}$$

$$c_2 = I_2 + 1 = \frac{1}{2}\left(\text{tr}(\mathbf{B}_s)^2 - \text{tr}(\mathbf{B}_s^2)\right), \tag{2.3b}$$

and the Cauchy stress is given as follows

$$\boldsymbol{\tau} = \frac{2}{\sqrt{c_2}}\left(\frac{\partial W_s}{\partial c_1}\mathbf{B}_s + c_2\frac{\partial W_s}{\partial c_2}\mathbf{P}\right). \tag{2.4}$$

The strain energy function of the neo-Hookean model [1] is given by

$$W_s = \frac{E_s}{6}\left(c_1 + \frac{1}{c_2} - 2\right), \tag{2.5}$$

and Skalak *et al.* [45] derived a strain energy function for red blood cells as

$$W_s = \frac{E_s}{8}\left(c_1^2 + \alpha c_2^2 - 2(\alpha+1)c_2 + \alpha + 1\right). \tag{2.6}$$

Here E_s is an elastic modulus, and α in (2.6) indicates the magnitude to suppress the surface dilation, which generally satisfies the condition $\alpha \gg 1$.

For red blood cells, there exists significant bending resistance that suppresses the formation of sharp edges. Following the bending model proposed by Pozrikidis [44], the bending stress $\mathbf{qn}$ is given by the transverse shear tension $\mathbf{q}$ and the unit normal vector $\mathbf{n}$, where $\mathbf{q}$ is given by the surface divergence of the bending moment tensor $\mathbf{m}$,

$$\mathbf{q} = ((\mathbf{P} \cdot \nabla) \cdot \mathbf{m}) \cdot \mathbf{P}. \tag{2.7}$$

The bending moment $\mathbf{m}$ is modeled by a linear constitutive law with bending stiffness E_b, which is expressed as

$$\mathbf{m} = E_b(\boldsymbol{\kappa} - \kappa_R\mathbf{P}), \tag{2.8}$$

where κ and κ_R are the current Cartesian curvature tensor and the reference mean curvature, given by

$$\kappa = -\mathbf{P} \cdot \nabla \mathbf{n} = -\nabla \mathbf{n}, \tag{2.9a}$$

$$\kappa_R = -\frac{1}{2}\text{tr}(\mathbf{P}_R \cdot \nabla \mathbf{n}_R) = -\frac{1}{2}\text{tr}(\nabla \mathbf{n}_R), \tag{2.9b}$$

respectively.

Combining the in-plane stress and the bending stress, the local force density vector $\mathbf{f}$ is given by the surface divergence of the membrane stress

$$\mathbf{f} = (\mathbf{P} \cdot \nabla) \cdot (\tau + q\mathbf{n}). \tag{2.10}$$

2.2 Full Eulerian formulation

2.2.1 Basic equations

We consider a whole domain Ω is separated into an inner domain Ω_1 and an outer domain Ω_2 by a closed interface (membrane) Γ, i.e. $\Omega = \Omega_1 \cup \Omega_2 \cup \Gamma$. Assuming that the velocity is continuous across the interface, the jump conditions $[*] = *_2 - *_1$ at the interface are given by the kinematic and dynamic conditions

$$[\mathbf{v}] = \mathbf{0}, \quad [\mathbf{n} \cdot \sigma] = \mathbf{f}_\Gamma, \tag{2.11}$$

where $\mathbf{v} = (v_1, v_2, v_3)$ is the velocity vector, σ the stress tensor, $\mathbf{n}$ the unit normal vector and $\mathbf{f}_\Gamma$ the surface singular force vector.

Assuming that the fluid is incompressible and Newtonian (with constant viscosity), the mixture equations without higher order terms are simply given as,

$$\nabla \cdot \mathbf{v} = 0, \tag{2.12a}$$

$$\rho\left(\frac{\partial \mathbf{v}}{\partial t} + \mathbf{v} \cdot \nabla \mathbf{v}\right) = -\nabla p + \nabla \cdot (2\mu \mathbf{D}(\mathbf{v})) + \oint_\Gamma \mathbf{f}_\Gamma \delta^{(3)}(\mathbf{x} - \mathbf{x}_\Gamma) d\Gamma, \tag{2.12b}$$

where p is the pressure, ρ the density, μ the dynamic viscosity, $\delta^{(3)}(\mathbf{x})$ the three-dimensional delta function and $\mathbf{D}(\mathbf{v}) = (\nabla \mathbf{v} + \nabla \mathbf{v}^T)/2$ the strain rate tensor. (2.12) is the standard formulation of the immersed boundary method.

To describe various physical and mathematical quantities in the inner and outer regions and on the interface in a full Eulerian approach, an indicator function is introduced as,

$$H(\mathbf{x}) = \begin{cases} 1, & \mathbf{x} \in \Omega_1, \\ 0, & \mathbf{x} \in \Omega_2. \end{cases} \tag{2.13}$$

The volume-fraction or volume-of-fluid (VOF) function over a small volume region $\delta V(\mathbf{x})$ is defined as follows

$$\phi(\mathbf{x}) = \frac{\int_{\delta V(\mathbf{x})} H(\mathbf{x}') dV'}{\int_{\delta V(\mathbf{x})} dV'}. \tag{2.14}$$

The singular force term in (2.12) can be replaced without using an explicitly-represented interface

$$\oint_{\Gamma} \mathbf{f}_{\Gamma} \delta^{(3)}(\mathbf{x} - \mathbf{x}_{\Gamma}) d\Gamma = \delta(\mathbf{x} - \mathbf{x}_{\Gamma}) \mathbf{f}(\mathbf{x}), \tag{2.15}$$

where $\delta(\mathbf{x})$ is the one-dimensional delta function given by $\delta(\mathbf{x} - \mathbf{x}_{\Gamma}) = |\nabla H(\mathbf{x})|$. Hereafter, we abbreviate $\delta(\mathbf{x})$ as δ. In the present approach, a following form is employed to include the singular force

$$\begin{aligned} \delta \mathbf{f} &= \delta(\mathbf{P} \cdot \nabla) \cdot (\boldsymbol{\tau} + \mathbf{qn}) \\ &= \nabla \cdot (\delta \boldsymbol{\tau} + \tilde{\mathbf{q}} \mathbf{n}), \end{aligned} \tag{2.16}$$

where $\tilde{\mathbf{q}}$ is a modified transverse shear tension vector with $\tilde{\kappa}_R = \delta \kappa_R$

$$\tilde{\mathbf{q}} = (\nabla \cdot \tilde{\mathbf{m}}) \cdot \mathbf{P}, \quad \tilde{\mathbf{m}} = E_b (\delta \boldsymbol{\kappa} - \tilde{\kappa}_R \mathbf{P}). \tag{2.17}$$

The reason to use the modified form is to reduce a numerical dissipation and suppress an oscillation of κ_R. This is described later. The detailed formula deformations of (2.16) and (2.17) are shown in Appendix A.

The surface left Cauchy-Green deformation tensor is required to evaluate the in-plane stress (2.4). Here we again consider (2.2) with the surface gradient tensor (2.1), then,

$$\begin{aligned} \mathbf{B}_s &= \mathbf{F}_s \cdot \mathbf{F}_s^T = \mathbf{P} \cdot \mathbf{F} \cdot \mathbf{P}_R \cdot \mathbf{P}_R^T \cdot \mathbf{F}^T \cdot \mathbf{P}^T \\ &= \mathbf{P} \cdot \mathbf{F} \cdot \mathbf{P}_R \cdot \mathbf{F}^T \cdot \mathbf{P} = \mathbf{P} \cdot \mathbf{G}_s \cdot \mathbf{P}, \qquad \mathbf{G}_s = \mathbf{F} \cdot \mathbf{P}_R \cdot \mathbf{F}^T, \end{aligned} \tag{2.18}$$

where, we use the relationship $\mathbf{P}_R = \mathbf{P}_R \cdot \mathbf{P}_R^T$. The material time derivative $(D/Dt = \partial/\partial t + \mathbf{v} \cdot \nabla)$ of $\mathbf{G}_s$ is given as,

$$\frac{D\mathbf{G}_s}{Dt} = \nabla \mathbf{v}^T \cdot \mathbf{G}_s + \mathbf{G}_s \cdot \nabla \mathbf{v},$$

by the material time derivatives of the reference surface projection tensor and the deformation gradient tensor,

$$\frac{D\mathbf{P}_R}{Dt} = \mathbf{0}, \quad \frac{D\mathbf{F}}{Dt} = \nabla \mathbf{v}^T \cdot \mathbf{F}.$$

In summary, the basic equations in the present Eulerian approach are given as follows

$$\frac{\partial \phi}{\partial t} + \mathbf{v} \cdot \nabla \phi = 0, \tag{2.19}$$

$$\nabla \cdot \mathbf{v} = 0, \tag{2.20}$$

$$\rho \left(\frac{\partial \mathbf{v}}{\partial t} + \mathbf{v} \cdot \nabla \mathbf{v} \right) = -\nabla p + \nabla \cdot (2\mu \mathbf{D}(\mathbf{v})) + \nabla \cdot (\delta \boldsymbol{\tau} + \tilde{\mathbf{q}} \mathbf{n}), \tag{2.21}$$

$$\frac{\partial \mathbf{G}_s}{\partial t} + \mathbf{v} \cdot \nabla \mathbf{G}_s = \nabla \mathbf{v}^T \cdot \mathbf{G}_s + \mathbf{G}_s \cdot \nabla \mathbf{v}, \tag{2.22}$$

$$\frac{\partial \tilde{\kappa}_R}{\partial t} + \mathbf{v} \cdot \nabla \tilde{\kappa}_R = -\tilde{\kappa}_R \mathbf{n} \cdot \nabla \mathbf{v} \cdot \mathbf{n}, \tag{2.23}$$

and

$$\mathbf{B}_s = \mathbf{P} \cdot \mathbf{G}_s \cdot \mathbf{P}, \quad \mathbf{P} = \mathbf{I} - \mathbf{n}\mathbf{n}.$$

Here, the unit normal vector and Cartesian curvature tensor are given by,

$$\mathbf{n} = \frac{\nabla \phi}{|\nabla \phi|}, \quad \kappa = -\nabla \left(\frac{\nabla \phi}{|\nabla \phi|} \right), \tag{2.24}$$

and the density and viscosity are written in a mixture form

$$\begin{cases} \rho = \phi \rho_1 + (1-\phi)\rho_2, \\ \mu = \phi \mu_1 + (1-\phi)\mu_2. \end{cases} \tag{2.25}$$

The surface in-plane stress and bending stress are given by (2.4) and (2.17), respectively. If Lagrangian marker points are provided to describe the interface, an analytical expression of the delta function smoothed at the grid size is often introduced to transfer quantities between the Lagrangian and Eulerian locations [10, 12, 14, 15, 18, 29, 40, 41, 51, 52]. In the full Eulerian approach, however, no Lagrangian marker is incorporated. Therefore, the delta function in (2.17) and (2.21) is evaluated in a different manner as detailed below.

In the present study, we introduce a smoothed indicator function in which the interface is expanded to its normal direction with a compactly supported region Γ (Fig. 1). Therefore, the VOF function has a smoothed profile on Γ. By considering the compactly supported region Γ, the one-dimensional delta function is smoothly approximated as,

$$\delta(\mathbf{x}) \approx |\nabla \phi|. \tag{2.26}$$

Same idea is also used in the continuum surface force (CSF) model [3].

Since $\kappa_R(\mathbf{X}(\mathbf{x},t))$ is a variable in a reference configuration, it cannot be directly obtained from $\phi(\mathbf{x},t)$ defined in a current configuration. Thus, $\kappa_R(\mathbf{X}(\mathbf{x},t))$ has to be updated as the state variable in the fully Eulerian method. Since the equation for updating $\kappa_R(\mathbf{X}(\mathbf{x},t))$ is an advection equation (2.27), we redefined $\tilde{\kappa}_R(\mathbf{x},t)$ as a variable in the current configuration with a convolution form

$$\int_{\delta V} \delta^{(3)}(\mathbf{x} - \mathbf{x}_\Gamma)\kappa_R(\mathbf{X}(\mathbf{x}_\Gamma,t))dV = \delta(\mathbf{x} - \mathbf{x}_\Gamma)\kappa_R(\mathbf{X}(\mathbf{x},t)) \approx |\nabla \phi(\mathbf{x},t)|\kappa_R(\mathbf{x},t),$$

which is approximated using a less dissipative numerical method (described later) to avoid the numerical diffusion, instead of updating κ_R itself. The updating equation (2.23) of $\tilde{\kappa}_R(\mathbf{x},t)$ is obtained by coupling the following equations

$$\frac{\partial \kappa_R}{\partial t} + \mathbf{v} \cdot \nabla \kappa_R = 0, \quad \frac{\partial |\nabla \phi|}{\partial t} + \mathbf{v} \cdot \nabla |\nabla \phi| = -|\nabla \phi|\mathbf{n} \cdot \nabla \mathbf{v} \cdot \mathbf{n}. \tag{2.27}$$
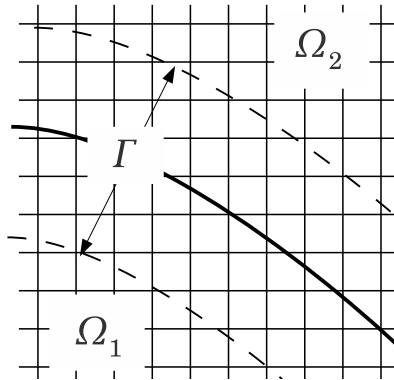
Figure 1: The compactly supported or smoothed interface region Γ immersed in the Cartesian mesh.

2.2.2 Discretization

A cubic computational domain is divided into a Cartesian coordinate mesh,

$$
\begin{aligned}
\delta V_{ijk} &= \delta x_i \times \delta y_j \times \delta z_k \\
&= [x_{i-1/2}, x_{i+1/2}] \times [y_{j-1/2}, y_{j+1/2}] \times [z_{k-1/2}, z_{k+1/2}],
\end{aligned}
\tag{2.28}
$$

for $i \in [1, N_x]$, $j \in [1, N_y]$, $k \in [1, N_z]$, where N_x, N_y, N_z is the total number of mesh points in each x, y, z direction. The variable location follows the staggered-grid arrangement shown in Fig. 2.
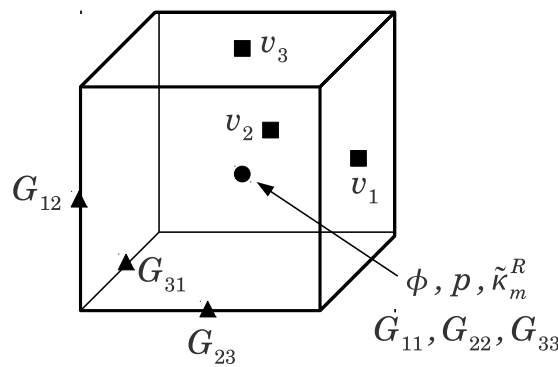

Figure 2: The variable locations on the staggered-grid.

Temporal discretization

Following the standard procedure of a projection type method [20], the variables are updated step-by-step. Hereafter, the superscripts n, $*$ and $n+1$ of a variable represent the time level of a current step, intermediate step and next step, respectively.

First, the VOF function ϕ and the reference curvature $\tilde{\kappa}_R$ are updated with the velocity $\mathbf{v}^n$ satisfying the divergence free condition

$$\frac{\phi^{n+1}-\phi^n}{\Delta t}+\frac{3}{2}\mathbf{v}^n\cdot\nabla\phi^n-\frac{1}{2}\mathbf{v}^{n-1}\cdot\nabla\phi^{n-1}=0, \tag{2.29}$$

$$\frac{\tilde{\kappa}_R^{n+1}-\tilde{\kappa}_R^n}{\Delta t}+\frac{3}{2}\mathbf{v}^n\cdot\nabla\tilde{\kappa}_R^n-\frac{1}{2}\mathbf{v}^{n-1}\cdot\nabla\tilde{\kappa}_R^{n-1}$$

$$=-\left(\frac{3}{2}\tilde{\kappa}_R^n\mathbf{n}^n\cdot\nabla\mathbf{v}^n\cdot\mathbf{n}^n-\frac{1}{2}\tilde{\kappa}_R^{n-1}\mathbf{n}^{n-1}\cdot\nabla\mathbf{v}^{n-1}\cdot\mathbf{n}^{n-1}\right). \tag{2.30}$$

Here, the second-order Adams-Bashforth method is applied. After this, the unit normal vector $\mathbf{n}$, Cartesian curvature tensor κ, surface projection tensor $\mathbf{P}$, mixture density ρ and viscosity μ at time step $n+1$ are calculated by using ϕ^{n+1}.

Next, the predicted velocity $\mathbf{v}^*$ is temporarily obtained by solving the equation of motion,

$$\rho^{n+1}\left(\frac{\mathbf{v}^*-\mathbf{v}^n}{\Delta t}+\frac{3}{2}\mathbf{v}^n\cdot\nabla\mathbf{v}^n-\frac{1}{2}\mathbf{v}^{n-1}\cdot\nabla\mathbf{v}^{n-1}\right)$$

$$=-\nabla p^n+\frac{1}{2}\nabla\cdot\left(2\mu^{n+1}\mathbf{D}(\mathbf{v}^n)+2\mu^{n+1}\mathbf{D}(\mathbf{v}^*)+\mathbf{T}^n\right)$$

$$+\frac{1}{2}\nabla\cdot\left(|\nabla\phi^{n+1}|(\boldsymbol{\tau}^n+\boldsymbol{\tau}^*)\right)+\nabla\cdot(\tilde{\mathbf{q}}^{n+1}\mathbf{n}^{n+1}). \tag{2.31}$$

Here, $\mathbf{T}$ is the stress increment which will be determined later. The second-order Adams-Bashforth method is applied to the advection term, and the Crank-Nicolson method is applied to the viscous stress and in-plane elastic stress. Following [25], the in-plane elastic stress at intermediate step $*$ is evaluated by a linear expansion of $\mathbf{G}_s$,

$$\boldsymbol{\tau}^*\approx\boldsymbol{\tau}^n+\mathbf{J}^n:\Delta\mathbf{G}_s^n, \tag{2.32}$$

with the fourth-order Jacobian tensor $\mathbf{J}$ at current step n defined as,

$$\mathbf{J}^n=\frac{\partial\boldsymbol{\tau}^n}{\partial\mathbf{G}_s^n}=\frac{\partial\boldsymbol{\tau}^n}{\partial\mathbf{B}_s^n}:\frac{\partial\mathbf{B}_s^n}{\partial\mathbf{G}_s^n}. \tag{2.33}$$

The detailed form of the fourth-order Jacobian tensor $\mathbf{J}$ is shown in Appendix B. From (2.22), $\Delta\mathbf{G}_s^n$ is approximately given as,

$$\Delta\mathbf{G}_s^n=\mathbf{G}_s^*-\mathbf{G}_s^n$$

$$\approx\frac{\Delta t}{2}\left((\nabla\mathbf{v}^n)^T\cdot\mathbf{G}_s^n+\mathbf{G}_s^n\cdot\nabla\mathbf{v}^n\right)+\frac{\Delta t}{2}\left((\nabla\mathbf{v}^*)^T\cdot\mathbf{G}_s^n+\mathbf{G}_s^n\cdot\nabla\mathbf{v}^*\right), \tag{2.34}$$

where the advection term is neglected as our preliminary study found that the effect of this term is insensitive to the overall projection procedure. By substituting (2.32) and

(2.34) into (2.31), a linear system for $\mathbf{v}^*$ is given by,

$$
\frac{\rho^{n+1}}{\Delta t}\mathbf{v}^* - \nabla \cdot \left(\mu^{n+1}\mathbf{D}(\mathbf{v}^*) + \frac{\Delta t}{4}|\nabla\phi^{n+1}|\mathbf{H}(\mathbf{v}^*,\mathbf{G}_s^n,\mathbf{J}^n) \right)
$$
$$
= \frac{\rho^{n+1}}{\Delta t}\mathbf{v}^n - \rho^{n+1}\left(\frac{3}{2}\mathbf{v}^n\nabla\mathbf{v}^n - \frac{1}{2}\mathbf{v}^{n-1}\nabla\mathbf{v}^{n-1} \right) - \nabla p^n + \frac{1}{2}\nabla \cdot (2\mu^{n+1}\mathbf{D}(\nabla\mathbf{v}^n) + \mathbf{T}^n)
$$
$$
+ \nabla \cdot \left(|\nabla\phi^{n+1}|\left(\boldsymbol{\tau}^n + \frac{\Delta t}{4}\mathbf{H}(\mathbf{v}^n,\mathbf{G}_s^n,\mathbf{J}^n) \right) + \tilde{\mathbf{q}}^{n+1}\mathbf{n}^{n+1} \right), \tag{2.35}
$$

where $\mathbf{H}(\mathbf{v},\mathbf{G}_s,\mathbf{J})$ is a second-order tensor defined as

$$
\mathbf{H}(\mathbf{v},\mathbf{G}_s,\mathbf{J}) = \mathbf{J} : \left((\nabla\mathbf{v})^T \cdot \mathbf{G}_s + \mathbf{G}_s \cdot \nabla\mathbf{v} \right),
$$

and its detailed form is shown in Appendix B.

Subsequently, we solve a Poisson equation for a scalar variable ψ by using the predicted velocity,

$$
\nabla \cdot \left(\frac{\nabla\psi^{n+1}}{\rho^{n+1}} \right) = \frac{\nabla \cdot \mathbf{v}^*}{\Delta t}. \tag{2.36}
$$

And the velocity and pressure are updated as follows

$$
\mathbf{v}^{n+1} = \mathbf{v}^* - \Delta t \frac{\nabla\psi^{n+1}}{\rho^{n+1}}, \tag{2.37}
$$

$$
p^{n+1} = p^n + \psi^{n+1}. \tag{2.38}
$$

The time-advancement of $\mathbf{T}^{n+1}$ is completed by substituting $\mathbf{v}^* = \mathbf{v}^{n+1} + \Delta t\psi^{n+1}/\rho^{n+1}$ into (2.31)

$$
\mathbf{T}^{n+1} = \Delta t\mu^{n+1}\left(\nabla\left(\frac{\nabla\psi^{n+1}}{\rho^{n+1}} \right) + \nabla\left(\frac{\nabla\psi^{n+1}}{\rho^{n+1}} \right)^T \right), \tag{2.39}
$$

and $\mathbf{G}_s$ is predicted with the divergence free velocity,

$$
\frac{\mathbf{G}_s^{n+1} - \mathbf{G}_s^n}{\Delta t} + \frac{3}{2}\mathbf{v}^n \cdot \nabla\mathbf{G}_s^n - \frac{1}{2}\mathbf{v}^{n-1} \cdot \nabla\mathbf{G}_s^{n-1}
$$
$$
= \frac{1}{2}\left((\nabla\mathbf{v}^n)^T + (\nabla\mathbf{v}^{n+1})^T \right) \cdot \mathbf{G}_s^n + \frac{1}{2}\mathbf{G}_s^n \cdot (\nabla\mathbf{v}^n + \nabla\mathbf{v}^{n+1}). \tag{2.40}
$$

The stability criteria for Δt is determined from the advection term, viscous term and membrane in-plane and bending stress terms. In the present method, an implicit approach [25] is adopted for the in-plane stress, however, it still imposes a stability limit due to nonlinearity. In all present simulations, Δt may be restricted by the stability condition of the membrane in-plane and bending stress terms even if the stability conditions of the advection and viscous terms defined as $\max(u)\Delta t/\Delta x$ and $\max(\mu/\rho)\Delta t/\Delta x^2$ are sufficiently less than 0.2 and 10, respectively. In conclusion, Δt is determined from the

trial and error approach because the determination of the exact stability condition for the membrane stress is not easy due to the nonlinear effect including the interfacial motion and its deformation. To obtain more precise stability condition based on the present implicit approach will be left as a topic for future work. As further attractive choices to stabilize the system, the efficient implicit approaches [5, 21, 22, 32, 36] would be considerable.

Spatial discretization

For the spatial discretization, the second-order central finite difference method is basically employed, but as an exception, the convection term in (2.30) is discretized by the kinetic energy conservation method [28], and the advection term in (2.39) is discretized by the third-order upwind finite volume (FV) method [2]. Meanwhile, to avoid the numerical dissipation and oscillation, a less dissipative numerical method, so-called interface capturing method is applied to the advection terms in (2.28) and (2.29). (The advection term in (2.39) should also be discretized by a less dissipative numerical method, but fortunately, since $\mathbf{G}_s$ has a smoothed profile near the interface, we apply the third-order FV method).

In the discretization, we adequately calculate a value from the neighborhood by the bi-linear interpolation. For example, we define the indices at cell node $i+\frac{1}{2}\ j+\frac{1}{2}\ k+\frac{1}{2}$ and cell center ijk, then a VOF function at the cell node is calculated as,

$$\phi_{i+\frac{1}{2}\ j+\frac{1}{2}\ k+\frac{1}{2}} = \frac{1}{8}\Big(\phi_{i\ j\ k}+\phi_{i+1\ j\ k}+\phi_{i\ j+1\ k}+\phi_{i+1\ j+1\ k}$$
$$+\phi_{i\ j\ k+1}+\phi_{i+1\ j\ k+1}+\phi_{i\ j+1\ k+1}+\phi_{i+1\ j+1\ k+1}\Big).$$

Note that in order to evaluate the elastic stress $\boldsymbol{\tau}$, we need to compute $\mathbf{G}_s$ only in the interface region Γ. In the fluid phase, a shearing motion gives rise to an elongation of a fluid element. Accordingly, some components of $\mathbf{G}_s$ tend to grow exponentially with time, resulting in an overflow of the computation [25, 34, 49]. To avoid such a numerical instability, we denote computational cells with $\delta_{ijk}h \geq \epsilon$, where $\delta_{ijk}h$ is a normalized approximate delta function, as interface regions, and therein reinitialize $\mathbf{G}_s^{n+1}$ to be the initial stretch-free condition $\mathbf{G}_s^{n+1}=\mathbf{P}^{n+1}$ in $\delta_{ijk}h < \epsilon$. The choice of ϵ depends on the problems and interfacial smoothness. In this study, we set the value of ϵ between 0.01 to 0.1. However, a profile of $\mathbf{G}_s$ is damped in the case that $\mathbf{G}_s^{n+1}$ is cut off or replaced with $\mathbf{P}^{n+1}$ outside of the interface in a moving interface problem. In the present study, a high order method (the 3rd order FV method) is applied to discretize the advection term to reduce numerical damping. However, problem still occurs for computations over longer time periods. For this reason, our numerical results certainly depend on the value of ϵ. As a future work, the extrapolation technique such as [46] should be incorporated into the present method to avoid the numerical damping and to increase the robustness.

A continuous interface capturing method

To be precise, the updating equation of the VOF function ϕ is derived from the advection equation of the indicator function H with the definition (2.14), as follows

$$\frac{\partial \phi}{\partial t} + \nabla \cdot (\mathbf{v}H) = \phi \nabla \cdot \mathbf{v}. \tag{2.41}$$

Here, from a numerical point of view, an accurate treatment is necessary to numerically obtain the flux $\mathbf{v}H$ without the numerical dissipation and oscillation. In other words, an accurate approximate function $\hat{H}$ is desirable for the indicator function H. In the discretization, the approximate function $\hat{H}$ is piecewisely reconstructed in a single mesh ijk, that is $\hat{H}_{ijk}$. In this study, from a requirement of the smoothed delta function, a continuous interface capturing method [24, 26], namely MTHINC method, is applied for the advection of ϕ and $\tilde{\kappa}_R$. We briefly introduce the MTHINC method below.

The continuous approximate function with a linear interface is introduced by using the hyperbolic tangent function,

$$\hat{H}_{ijk}(\mathbf{x}) = \frac{1}{2}\left(1 + \tanh(\beta'(\mathbf{n}_{ijk} \cdot \mathbf{x} + d_{ijk}))\right), \tag{2.42}$$

where $\mathbf{n} \cdot \mathbf{x} + d = 0$ indicates the implicit representation of the interface, and $\beta' = \beta/h$ is a parameter to decide a sharpness of the interface, which depends on a problem. (In this paper, $\beta = 1$ is employed). Here, h is a characteristic length, and it is given as $h = \Delta x = \Delta y = \Delta z$ in a uniform Cartesian mesh, thus it is found that the approximate function (2.41) approaches to the exact indicator function (or Heaviside function) as grid resolution increase. The normal vector defined in (2.24) is calculated by the Youngs estimation [57, 58] from the instantaneous VOF function. Then d_{ijk} in (2.41) is decided by a constraint,

$$\phi_{ijk} = \frac{1}{\Delta x_i \Delta y_j \Delta z_k} \int_{\delta x_i} dx \int_{\delta y_j} dy \int_{\delta z_k} dz \hat{H}_{ijk}(\mathbf{x}). \tag{2.43}$$

Since the VOF function is solved with the numerical flux estimated by the approximate function (2.41), it is expected the numerical result smoothly distributes over a few computational meshes, but not dissipative over time. For a more detailed description, we refer the readers to [24, 26].

In this paper, we propose an advection method for a singular quantity defined at the interface, following the idea of the MTHINC method. The advection term in (2.29) is rewritten to,

$$\frac{\partial \tilde{\kappa}_R}{\partial t} + \mathbf{v} \cdot \nabla \tilde{\kappa}_R = 0$$

$$\rightarrow \frac{\partial \tilde{\kappa}_R}{\partial t} + \nabla \cdot (\mathbf{v}\tilde{\kappa}_R) = \tilde{\kappa}_R \nabla \cdot \mathbf{v}$$

$$\rightarrow \frac{\partial \tilde{\kappa}_R}{\partial t} + \nabla \cdot (\mathbf{v}G) = \tilde{\kappa}_R \nabla \cdot \mathbf{v}, \tag{2.44}$$

where $G(\mathbf{x})$ is a function to describe the profile $\tilde{\kappa}_R$. Using approximate function (2.41), the piecewise approximate function $\hat{G}_{ijk}(\mathbf{x}) \approx G(\mathbf{x})$, $\mathbf{x} \in \delta V_{ijk}$ is prescribed as,

$$\hat{G}_{ijk}(\mathbf{x}) = c_{ijk}|\nabla H_{ijk}(\mathbf{x})| = c_{ijk}\frac{\beta'}{2}\left(1 - \tanh^2(\beta'(\mathbf{n}_{ijk} \cdot \mathbf{x} + d_{ijk}))\right), \qquad (2.45)$$

where, by using the constraint,

$$(\tilde{\kappa}_R)_{ijk} = \frac{1}{\Delta x_i \Delta y_j \Delta z_k}\int_{\delta x_i} dx \int_{\delta y_j} dy \int_{\delta z_k} dz \hat{G}_{ijk}(\mathbf{x}), \qquad (2.46)$$

coefficient c_{ijk} is uniquely determined as,

$$c_{ijk} = \frac{\Delta x_i \Delta y_j \Delta z_k (\tilde{\kappa}_R)_{ijk}}{\int_{\delta x_i} dx \int_{\delta y_j} dy \int_{\delta z_k} dz |\nabla H_{ijk}(\mathbf{x})|}. \qquad (2.47)$$

The volume integration in (2.46) is numerically estimated with the eight-point Gaussian quadrature.

In the original MTHINC method, a semi-Lagrangian updating way with a directional splitting approach is adopted to update the VOF function. In this paper, the second-order Adams-Bashforth method is adopted for simplicity. The flux divergence terms $\nabla \cdot (\mathbf{v}H)$ in (2.40) and $\nabla \cdot (\mathbf{v}G)$ in (2.43) are calculated by the Gauss divergence theorem. In a Cartesian coordinate mesh, it is simply written as,

$$\nabla \cdot (\mathbf{v}H)_{ijk} \approx \nabla \cdot (\mathbf{v}\hat{H})_{ijk} = \frac{1}{\Delta x_i}\left((v_1\overline{H})_{i+\frac{1}{2}jk} - (v_1\overline{H})_{i-\frac{1}{2}jk}\right)$$
$$+ \frac{1}{\Delta y_j}\left((v_2\overline{H})_{ij+\frac{1}{2}k} - (v_2\overline{H})_{ij-\frac{1}{2}k}\right) + \frac{1}{\Delta z_k}\left((v_3\overline{H})_{ijk+\frac{1}{2}} - (v_3\overline{H})_{ijk-\frac{1}{2}}\right), \quad (2.48)$$

where $\overline{H}$ indicates an area integrated average value on a mesh boundary for the function $\hat{H}(\mathbf{x})$ which is reconstructed on a cell by an upwind direction of a cell-boundary velocity, and we adopt the four-point Gaussian quadrature.

3   Numerical results

We apply the SOR method for solving the linear system (2.34). In this study, same density is prescribed for both fluid phases, therefore, the pressure Poisson equation (2.35) can be solved by the FFT method for a periodic boundary.

In the present paper, the iteration in the SOR method is carried on until the iterative error between (k) and $(k+1)$ iterative steps determined as,

$$E^{(k+1)} = \sqrt{\frac{\sum_{i,j,k}(v_{1ijk}^{(k+1)} - v_{1ijk}^{(k)})^2 + \sum_{i,j,k}(v_{2ijk}^{(k+1)} - v_{2ijk}^{(k)})^2 + \sum_{i,j,k}(v_{3ijk}^{(k+1)} - v_{3ijk}^{(k)})^2}{\sum_{i,j,k}(v_{1ijk}^{(0)})^2 + \sum_{i,j,k}(v_{2ijk}^{(0)})^2 + \sum_{i,j,k}(v_{3ijk}^{(0)})^2}},$$

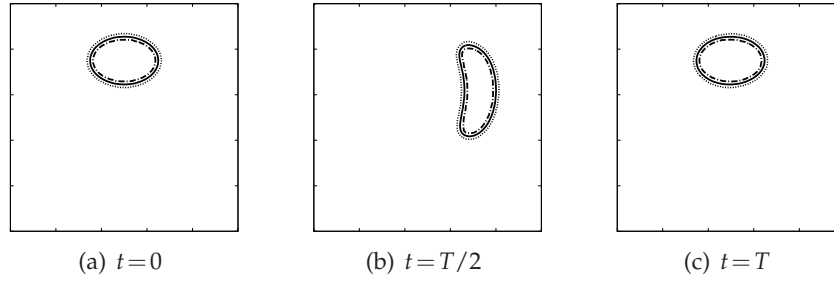is less than a criteria 10^{-6}, and an acceleration parameter is set to 1.4.

(a) $t\!=\!0$ (b) $t\!=\!T/2$ (c) $t\!=\!T$

Figure 3: Development of the VOF function in the advection problem on a single vortex flow field. The contours are shown at $\phi\!=\!0.05$ (dotted line), 0.5 (solid line) and 0.95 (dashed line).

3.1 Accuracy of the interface capturing method

First, we check the numerical accuracy of the MTHINC method including the advection of the reference mean curvature. A validation is carried out on a 2-D domain $[0,1]^2$ with an initial elliptic interface,

$$\frac{(x-0.5)^2}{a^2}+\frac{(y-0.75)^2}{b^2}=1,$$

where $a\!=\!0.15$ and $b\!=\!0.7a$. A time-dependent stream function

$$\Psi(x,y,t)=\frac{1}{\pi}\sin^2(\pi x)\cos^2(\pi y)\cos\left(\frac{\pi t}{T}\right),$$

is imposed, where T is a period at which the solution returns to the initial configuration, and $T\!=\!1$ is used in this test. Here, the initial mean curvature is analytically given by the elliptic interface. The maximum CFL (Courant-Friedrichs-Lewy) number is set to 0.25.

The numerical results of the VOF function on $N(=N_x=N_y)=128$ mesh are shown in Fig. 3. The interface is most deformed at $t\!=\!T/2$, after that it becomes an elliptic-like shape at $t\!=\!T$. Since the interval between each contour-line at $\phi\!=\!0.05$, 0.5 and 0.95 does not spread even at $t\!=\!T$, it is confirmed that the VOF profile is not smeared out over time. In Fig. 4, we also show the profile of the reference mean curvature convolved with
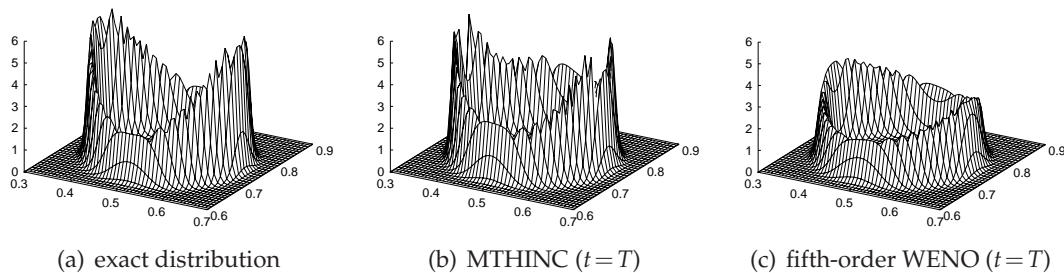

(a) exact distribution   (b) MTHINC ($t\!=\!T$)   (c) fifth-order WENO ($t\!=\!T$)

Figure 4: The exact distribution and numerical solutions on $N\!=\!128$ mesh after one period ($t\!=\!T\!=\!1$) for the reference mean curvature convolved with the normalized delta function: $\kappa_R\overline{\delta}$. The solution based on the fifth-order WENO method [27] is obtained for the reference mean curvature κ_R itself without convolution, and it is plotted by multiplying $\overline{\delta}$.

Table 1: Numerical errors in L_1, L_2 and L_∞ norms and the respective convergence rates in the advection problem on a time-dependent single vortex flow field after one period ($t = T = 1$).

	N	L_1 Error	Order	L_2 Error	Order	L_∞ Error	Order
ϕ	32	2.67E-3	–	9.82E-3	–	1.02E-1	–
	64	1.01E-3	1.40	5.15E-3	0.93	7.54E-2	0.44
	128	4.35E-4	1.22	3.20E-3	0.69	6.10E-2	0.31
	256	2.03E-4	1.10	2.13E-3	0.59	5.96E-2	0.03
$\kappa_R \bar{\delta}$	32	5.66E-2	–	2.12E-1	–	2.01E-0	–
	64	2.03E-2	1.48	1.09E-1	0.96	1.56E-0	0.37
	128	6.80E-3	1.58	5.22E-2	1.06	1.05E-0	0.57
	256	2.39E-3	1.51	2.49E-2	1.07	6.88E-1	0.61

a normalized approximate delta function, $\kappa_R \bar{\delta}$, where $\bar{\delta} = \delta \Delta x$. Here, the approximate delta function δ itself depends on the mesh resolution, thus, we discuss a normalized quantity $\delta \Delta x$. As shown in Fig. 4(a), the initial convolved curvature smoothly distributes over a few computational meshes as well as the smoothed VOF function. The solution based on the present approach at $t = T$ shown in Fig. 4(b) agrees with the exact solution well while the maximum value is only slightly reduced due to numerical dissipation. By comparison, the solution based on the fifth-order WENO method [27] suffers more serious numerical dissipation. As shown in Fig. 4(c), the solution is smeared out over time, as a result, the curvature distribution along the surface is hidden.

The convergence rates to the spatial resolution for ϕ and $\kappa_R \bar{\delta}$ are shown in Table 1. The number of mesh points is doubly increased from $N = 32$ to $N = 256$. The errors are measured by the L_1, L_2 and L_∞ norms which are defined for a quantity q as follows

$$L_1(q) = \frac{\sum_{i,j,k} |q_{ijk}^{(n)} - q_{ijk}^{(e)}|}{N_x N_y N_z}, \quad L_2(q) = \sqrt{\frac{\sum_{i,j,k} (q_{ijk}^{(n)} - q_{ijk}^{(e)})^2}{N_x N_y N_z}}, \quad L_\infty(q) = \max_{i,j,k} |q_{ijk}^{(n)} - q_{ijk}^{(e)}|, \quad (3.1)$$

where $q^{(n)}$ and $q^{(e)}$ are the numerical solution and exact solution, respectively. The convergence rate of the local error L_∞ is worse than that of the global errors L_1, L_2 because the VOF function and its gradient are only smooth within a compactly supported region Γ. Whereas, the global L_1 errors for ϕ and $\kappa_R \bar{\delta}$ converge with a rate of 1 and 1.5, respectively. It is expected the MTHINC method and the present convolution approach adequately work on a full Eulerian interaction method.

As discussed in [8, 13, 16, 35, 42], it is a well known problem that the local error of the curvature does not converge in a way based on a smoothed VOF (or density/color) function even if the mesh resolution is increased. We have confirmed that in the interface region the error is order one for a 2D circular interface, therefore does not converge ($\approx \mathcal{O}(\Delta x^0)$). It is a crucial issue to correctly model the membrane elastic (bending) force, and obtain an accurate estimation for the curvature. This will be left as an topic for future work.

3.2 Deformation due to an external surface force

A spherical membrane with a radius of 0.1 is centrally-located on a 3-D domain $[0,1] \times [0,1] \times [0,0.5]$. The neo-Hookean model (2.5) is employed and the bending effect is neglected in this test. An external surface force $\mathbf{F}_b$ is taken into account in the equation of motion (2.21) as a singular body force,

$$\mathbf{F}_b = -\delta \mathrm{sgn}(z-0.25)\gamma \mathbf{e}_z,$$

for $t \leq 0.5$, where $\mathrm{sgn}(x)$ is the sign function, $\mathbf{e}_z = (0,0,1)$ the unit vector in the vertical direction, and γ the constant which is prescribed as $\gamma = 4$, in this study. Due to the imposed vertical force, the spherical capsule is vertically squashed without changing the volume. After that, by releasing the imposed force $\mathbf{F}_b$, the squashed capsule is expected to recover to an initial sphere satisfying a stress-free condition. The periodic boundary condition is imposed on both x and y boundaries, and the no-slip condition is imposed on the z walls. The fluid properties are set to the same values, where density and viscosity are 1 and 0.2, respectively, and the elastic modulus $E_s = 5$ is prescribed. The time increment depends on the mesh and specified as $\Delta t = 0.02 \times (16/N_x)^2$.

First, we show the behavior of the interface on the $N_x = 128$ mesh in Fig. 5, and also show the y-component vorticity and pressure in cross-section. The spherical membrane is deformed due to the external force until $t = 0.5$ as expected. The velocity is dissipated by the viscous stress, but the pressure in the membrane increases to balance with the membrane stress. After releasing the imposed force, the interfacial shape approaches to the spherical shape, then it seems to recover to a perfect sphere at $t = 2$.

In this problem, the kinetic energy $E_{kinetic} = \rho \mathbf{v}^2/2$, the elastic strain energy $E_{elastic} = W_s$, the energy dissipation of the viscous stress

$$E_{viscous} = \int_t \mu \nabla \mathbf{v} : \nabla \mathbf{v} dt$$

and the energy input of the body force

$$E_{body} = -\int_t \mathbf{v} \cdot \mathbf{F}_b dt$$

contribute to the energy transfer process, then the summation of energy over the computational domain is plotted in Fig. 6. The kinetic energy is relatively small compared with other energy contributions, but it increases just after the initial step and releasing the body force at $t = 0.5$. Whereas, the potential energy of the membrane gradually increases and is to balance with the body force until $t = 0.5$, and after releasing the body force, it rapidly decreases and approaches to zero which is a stress-free state. Here, with taking notice of the numerical conservation for the total energy

$$\int_\Omega d\Omega E_{total} = \int_\Omega d\Omega (E_{kinetic} + E_{elastic} + E_{viscous} + E_{body}),$$

(a) $t=0$ (b) $t=0.1$

(c) $t=0.5$ (d) $t=0.7$

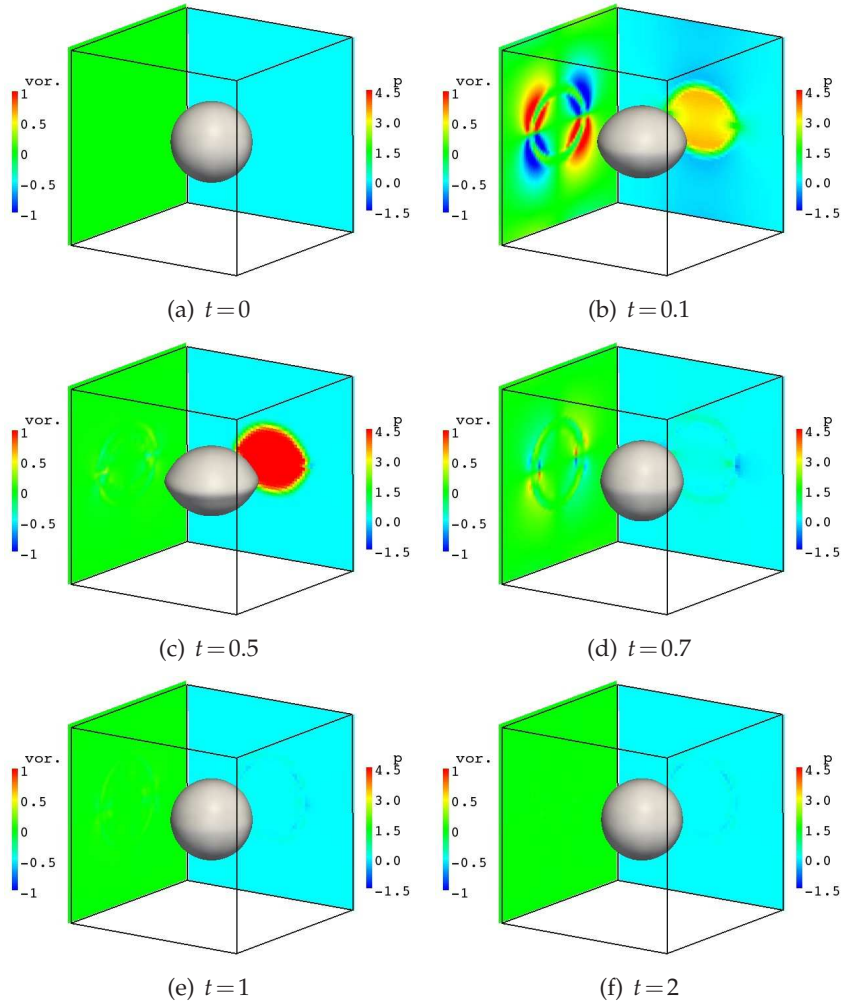(e) $t=1$ (f) $t=2$

Figure 5: The instantaneous solutions in the deformed capsule problem. The external force is imposed on the membrane surface until $t=0.5$. The figures are shown within a range of $[0.25,0.75]\times[0.25,0.75]\times[0,0.5]$, with respect to the isosurface of the VOF function at $\phi=0.5$, y-component vorticity in $x-z$ cross-section on $y=0.5$, and pressure in $y-z$ cross-section on $x=0.5$.

it remains within a level of 10^{-4}. The energy conservation is one of the important issues for the shape reversibility. Further, the deformation modes of a spherical surface harmonics are useful indicators of shape reversibility. Using zenith angle θ and azimuth angle φ, the radial function $r(\theta,\varphi)$ is expanded as,

$$r(\theta,\varphi)=\sum_{n=0}\left(R_{n,0}\mathcal{P}_{n,0}(\cos\theta)\right.$$

$$\left.+\sum_{m=1}^{n}\left(R_{n,m}^{(c)}\mathcal{P}_{n,m}(\cos\theta)\cos(m\varphi)+R_{n,m}^{(s)}\mathcal{P}_{n,m}(\cos\theta)\sin(m\varphi)\right)\right), \qquad (3.2)$$
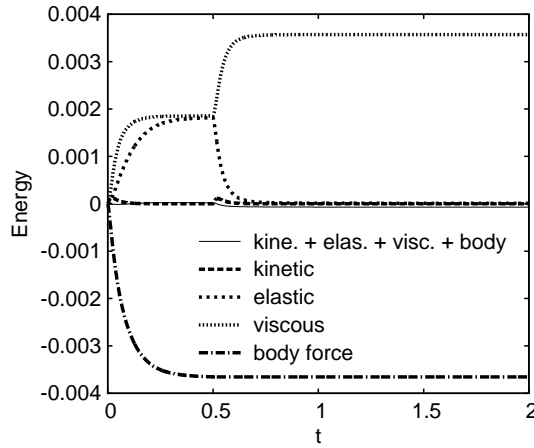
Figure 6: The time history of the energy summarized over the computational domain.

where $\mathcal{P}_{n,m}$ is the normalized associated Legendre polynomials. Following a description in [49], the expansion coefficients $R_{n,0}$, $R_{n,m}^{(c)}$ and $R_{n,m}^{(s)}$ are estimated on the Eulerian mesh.

$$R_{n,0} \approx \frac{1}{\sqrt{2\pi}} \sum_{i,j,k} \delta_{ijk} \mathcal{P}_{n,0}(\cos\theta_{ijk}) \Delta x_i \Delta y_j \Delta z_k, \tag{3.3a}$$

$$R_{n,m}^{(c)} \approx \frac{1}{\sqrt{\pi}} \sum_{i,j,k} \delta_{ijk} \mathcal{P}_{n,m}(\cos\theta_{ijk}) \cos(m\varphi_{ijk}) \Delta x_i \Delta y_j \Delta z_k, \tag{3.3b}$$

$$R_{n,m}^{(s)} \approx \frac{1}{\sqrt{\pi}} \sum_{i,j,k} \delta_{ijk} \mathcal{P}_{n,m}(\cos\theta_{ijk}) \sin(m\varphi_{ijk}) \Delta x_i \Delta y_j \Delta z_k, \tag{3.3c}$$

where the angle is calculated by,

$$\theta_{ijk} = \cos^{-1}\left(\frac{z_{ijk} - z_c}{|\mathbf{x}_{ijk} - \mathbf{x}_c|}\right), \quad \varphi_{ijk} = \tan^{-1}\left(\frac{y_{ijk} - y_c}{x_{ijk} - x_c}\right), \tag{3.4}$$

with the numerically-obtained centroid $\mathbf{x}_c$ from the VOF function ϕ as follows.

$$\mathbf{x}_c = \frac{\sum_{ijk} \phi_{ijk} \mathbf{x}_{ijk} \Delta x_i \Delta y_j \Delta z_k}{\sum_{ijk} \phi_{ijk} \Delta x_i \Delta y_j \Delta z_k}. \tag{3.5}$$

The time history of the modal amplitudes $|R_{n,0}| = \sqrt{(R_{n,0}^{(c)})^2 + (R_{n,0}^{(s)})^2}$ with $n = 0,2,4,6$ is shown in Fig. 7. It is found that the second-order mode relating to an ellipsoidal mode is relatively large, but higher order modes ($n \geq 4$) are also observed during the force imposing ($t \leq 0.5$). After releasing the external force, all modes are to vanish over time except for a basic spherical mode $n = 0$. This suggests that the deformed membrane adequately recovers to the initial sphere without any deformation. We also plot the time history of
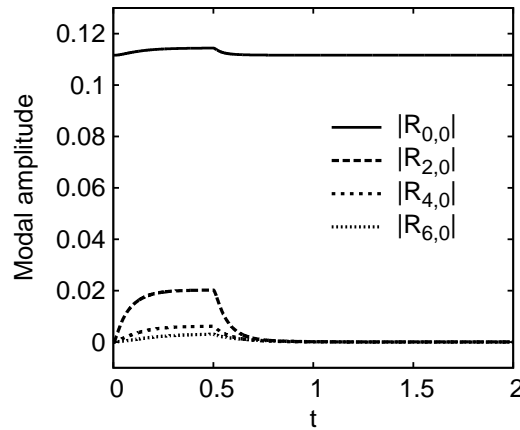
Figure 7: The time history of the modal amplitudes $n=0,2,4,6$ and $m=0$ for the spherical surface harmonics.
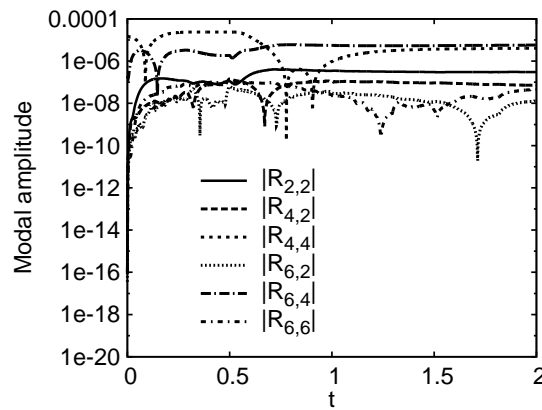

Figure 8: Same as Fig. 7, but the order of the spherical surface harmonics is for $m=2,4,6$.

the modal amplitude $|R_{n,m}| = \sqrt{(R_{n,m}^{(c)})^2 + (R_{n,m}^{(s)})^2}$ for $n=2,4,6$ with non-zero m in Fig. 8. Since the mth-order modes for $(m > 1)$ represent perturbations distributed over the azimuth angle φ, they are small in this numerical configuration. Thus it is not surprising that even on a Cartesian mesh, we are able to maintain axisymmetry numerically.

Here, the relative errors are computed using a set of the doubly-refined meshes as $(N_x^{(coarse)}, N_x^{(fine)}) = (16,32), (32,64), (64,128)$ and $(128,256)$, and the convergence rates are investigated with the grid refinement. The numerical errors measured by (3.1) at $t=0.1$ for the VOF function, velocity and pressure are shown in Table 2. The velocity error is averaged from each component as: $L_{1,2,\infty}(\mathbf{v}) = (L_{1,2,\infty}(v_1) + L_{1,2,\infty}(v_2) + L_{1,2,\infty}(v_3))/3$. It is well known that the error under the L_1 norm normally behaves better than that using the L_∞ norm. Our solution indicates that the L_1 error adequately converges with the first-order accuracy, but the convergence rate for the L_∞ error is less than 1 even though a second-order spatial discretization is applied. We believe that the main contributing

Table 2: Numerical errors in L_1, L_2 and L_∞ norms and the respective convergence rates in the deformed capsule problem at $t=0.1$. The relative errors are computed using a set of the doubly-refined meshes as $(N_x^{(coarse)}, N_x^{(fine)}) = (16,32)$, $(32,64)$, $(64,128)$ and $(128,256)$.

		L_1		L_2		L_∞	
	N_x	Error	Order	Error	Order	Error	Order
ϕ	16	7.02E-3	–	2.28E-2	–	1.25E-1	–
	32	2.73E-3	1.36	1.50E-2	0.61	1.42E-1	-0.19
	64	1.27E-3	1.11	1.04E-2	0.52	1.50E-1	-0.08
	128	6.22E-4	1.03	7.34E-3	0.50	1.67E-1	-0.15
v	16	1.96E-3	–	3.40E-3	–	1.70E-2	–
	32	9.89E-4	0.99	2.11E-3	0.69	1.49E-2	0.19
	64	4.89E-4	1.02	1.21E-3	0.80	1.44E-2	0.05
	128	2.59E-4	0.91	6.90E-4	0.81	1.04E-2	0.47
p	16	8.19E-2	–	2.11E-1	–	2.77E-0	–
	32	4.07E-2	1.01	1.59E-1	0.41	3.22E-0	-0.21
	64	1.88E-2	1.12	7.89E-2	1.01	1.68E-0	0.93
	128	1.02E-2	0.88	5.17E-2	0.61	1.90E-0	-0.18

factor is the lack of accuracy of the current method for estimating the normal vector of the interface [8, 13, 16, 35, 42]. The other main factor is due to the approximation of the delta function [29, 30, 33]. Possible improvements might be possible by incorporating the ideas of the level set method [39, 47] and the immersed interface method [30, 31, 33].

3.3 A deformable spherical capsule in a shear flow

We consider a spherical capsule with a radius of $a=1$, obeying the neo-Hookean law, in a computational domain $x \in [-4,4], y \in [-2,2], z \in [-4,4]$. The opposite velocities $\pm V$ that result in a shear rate $\dot{\gamma} = 2U/H_z = U/4$ are imposed on the top and bottom walls in z direction. The periodic boundary condition is imposed on other x and y directions. Here, same viscosity is specified for both fluid phases. The viscosity is given by Reynolds number $Re = \rho \dot{\gamma} a^2 / \mu$, and the membrane stiffness is given by capillary number $Ca = \mu \dot{\gamma} a / E_s$. In this test, $\rho = 1$, $\dot{\gamma} = 1$ and $Re = 0.01$ are fixed, therefore the membrane stiffness only depends on the capillary number.

3.3.1 Effect of the elastic stiffness

Here, we neglect the bending force, and the capillary number is varied as 0.0125, 0.025, 0.05, 0.1 and 0.2. First, we show the numerical result with the number of mesh points $(N_x, N_y, N_z) = (128, 64, 128)$ and the time increment $\Delta t = 0.001$. The isosurface of the VOF function is shown in Fig. 9. As expected, the deformation becomes larger as the capillary number increases. Taylor [50] introduces a deformation parameter $D = (l-s)/(l+s)$ for specifying the interfacial deformation in the vertical cross-section, with fitting to an ellipse. Here, l and s denote the semi-major and semi-minor axes of the ellipse respec-

(a) $Ca = 0.0125$ (b) $Ca = 0.025$ (c) $Ca = 0.05$
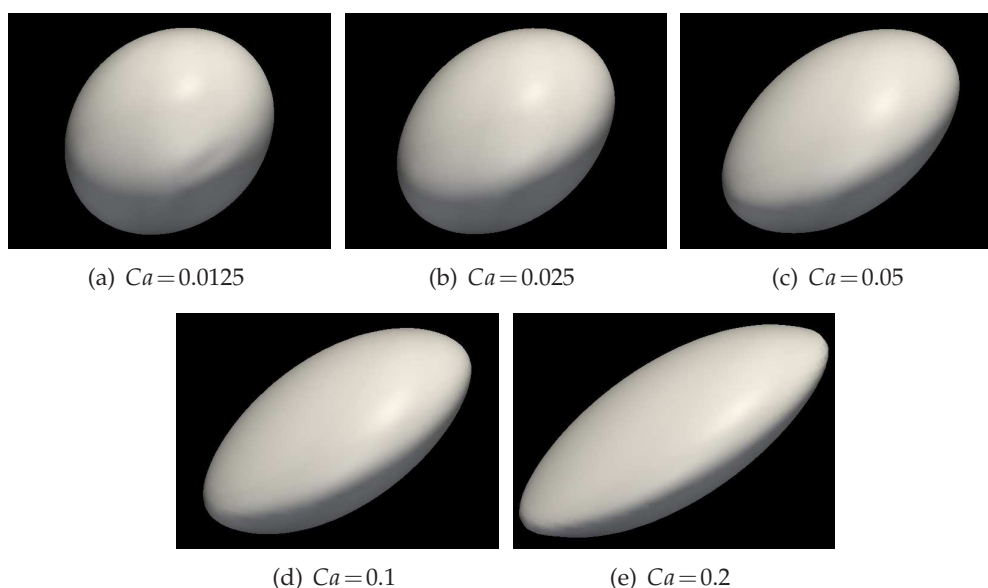
(d) $Ca = 0.1$ (e) $Ca = 0.2$

Figure 9: The fully-developed deformed surface of the neo-Hookean membrane subjected to the linear shear flow for various capillary numbers.

tively. The interface is explicitly expressed as the coordinate points picked up from the cross points between the contour line of the VOF function at $\phi = 0.5$ and the computational meshes. It has been reported in many literatures that the shape of the interface in a cross section almost remains ellipsoidal even in $Ca = 0.2$ (e.g., [10, 43]). The shape of the interface in a cross section is fitted to the general elliptic equation: $ax^2 + by^2 + cxy + dx + ey + 1 = 0$, using the least-squares method, and the major and minor axes are calculated. The time history of the deformation parameter D with different capillary numbers is shown in Fig. 10. In this regard, the solutions are obtained by increasing the number of mesh points as $N_x = 64$, 128 and 256, in addition, the numerical solutions obtained by the immersed boundary method [10] and the boundary element method [43] are also shown. The mesh-dependent time increment is used to be $\Delta t = 0.001 \times (128/N_x)^2$. It is confirmed that the shape converges to a steady-state over time, however, the results of the present full Eulerian method are slightly different from those of the immersed boundary method [10] in which the Eulerian mesh for a fluid and the Lagrangian mesh for a membrane are used, especially within the range of small deformation. This is because the full Eulerian approach essentially involves a numerical dissipation for the advection term. In this simulation, the membrane stress may be underestimated or the deformation may be overestimated. However, the effect of numerical dissipation is reduced significantly when a relatively fine mesh ($N_x = 256$) is used as our solution agrees well with previous solutions obtained in [10, 43]. We confirmed that in the transport of the overall kinetic-energy for the cases of $Ca = 0.1$ and $Ca = 0.2$, the variation of its time derivative is sufficiently smaller than those of the energy input rate, the energy dissipation rate and the strain energy rate,
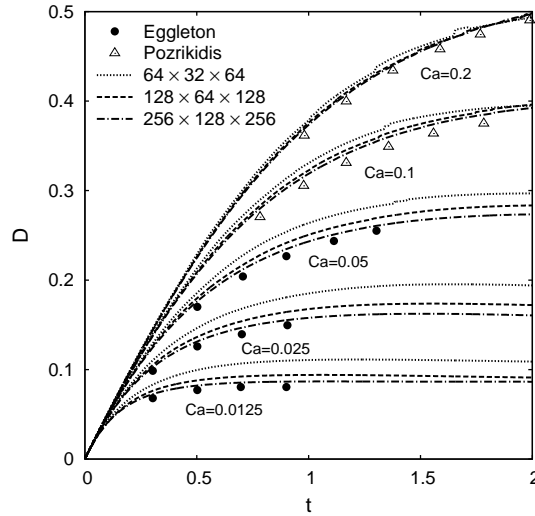
Figure 10: The Taylor deformation parameter D vs. time t for various capillary numbers. The lines are the present solution on $N = 64$, 128, 256 meshes, the filled-circles indicate the solutions by means of the immersed boundary method by Eggleton *et al.* [10], and open-triangles show those of the boundary element method by Pozrikidis [43].

indicating that one may regard the transient capsule deformation as taking place in a quasi-steady velocity field. Therefore, the good agreement with the results of [43], in which the steady Stokes equation is solved, is reasonable.

3.3.2 Effect of the bending stiffness

Next, the effect of the bending stiffness is studied. According to [32,44], a modified bending modulus defined as $E'_b = E_b / (a^2 E_s)$ is varied as 0.01, 0.025 and 0.0375 with the capillary number $Ca = 0.05$. In this case, the bending stiffness is dominant in stability, therefore, a small time step size $\Delta t = 6.25 \times 10^{-5}$ is used. The computation is carried out until $t = 2$ on $N_x = 128$ mesh. The time history of the deformation parameter is again plotted in Fig. 11. With increasing the bending stiffness, the deformation is to be moderated. The tendency of the present result shows good agreement with the boundary element method [44] and the immersed boundary method [32].

3.4 Pressure-driven flow with the biconcave capsules

Finally, we consider the biconcave capsules replicating the geometry of red blood cell (RBC) within capillary parallel plates with a periodic boundary, and prescribe a pressure gradient as a body force $-\Delta P / L \mathbf{e}_x$ to a streamwise direction x. According to [11], a single biconcave shape is given as,

$$\frac{x - x_c}{a} = \pm \frac{1}{2} \left(c_1 + c_2 \sigma + c_3 \sigma^2 \right) \sqrt{1 - \sigma}, \quad \sigma = \frac{(y - y_c)^2 + (z - z_c)^2}{a^2},$$
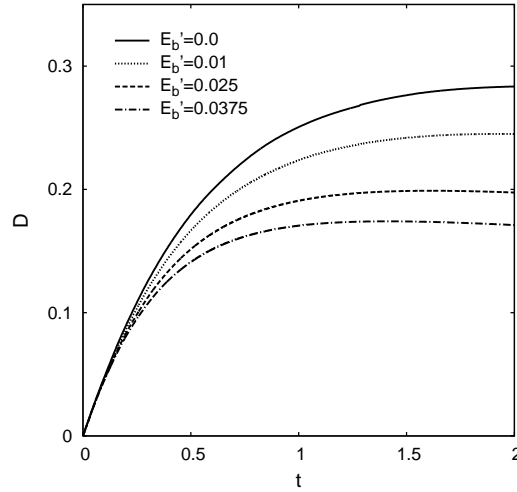
Figure 11: The effect of the bending stiffness on the Taylor deformation parameter D. E'_b is the normalized bending stiffness defined as $E'_b = E_b(a^2/E_s)$.

where (x_c, y_c, z_c) is the central position, a the representative capsule size, and a set of parameters $c_1 = 0.35$, $c_2 = 2.003$ and $c_3 = -1.123$ are used. In this simulation, each membrane is modeled by the Skalak model (2.6).

3.4.1 Investigation of the surface dilation

A computational domain $[0,0.5]^3$ is divided into $N^3 = 64^3$ meshes, and the wall boundary condition is imposed on the spanwise direction y. The same density $\rho_1 = \rho_2 = 1$ is used for both fluid phases, and the viscosities are set to $\mu_1 = 0.25$ and $\mu_2 = 0.05$ for both inside and outside of a membrane, respectively. In this regard, Reynolds number based on the domain height is approximately 4. The elastic stiffness $E_s = 0.05$ and bending stiffness $E_b = 5 \times 10^{-5}$ are fixed, and the pressure gradient is set to -1. The time step size Δt is prescribed as 0.001.

In the Skalak model [45], a surface dilation is controlled by a constraint coefficient. As a first step, we check the effect of the surface dilation magnitude α in (2.6), by setting α to 2, 10 and 40. A single biconcave capsule with a radius of $a = 0.17$ is located at a center position. In the Eulerian approach, the membrane surface is not explicitly given, thus we make use of a following relationship.

$$s = \int_{\delta V} \delta dV \ \rightarrow \ \frac{Ds}{Dt} = -\int_{\delta V} \delta \mathbf{n} \cdot \nabla \mathbf{v} \cdot \mathbf{n} dV, \tag{3.6}$$

where, s is a total surface area. Then, the total surface area is numerically estimated by,

$$s^{n+1} = s^n - \Delta t \sum_{i,j,k} \Delta x_i \Delta y_j \Delta z_k \delta^n_{ijk} \mathbf{n}^n_{ijk} \cdot \nabla \mathbf{v}^n_{ijk} \cdot \mathbf{n}^n_{ijk}. \tag{3.7}$$
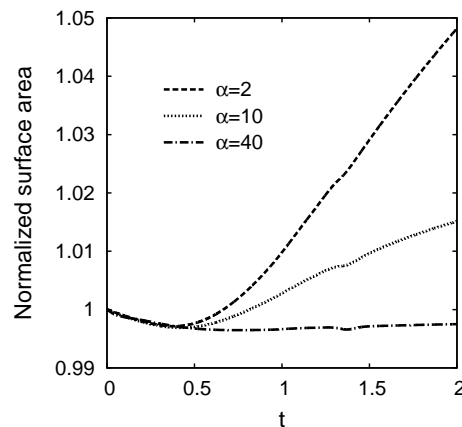
Figure 12: The effect of the surface dilation coefficient in Skalak model (2.6). The normalized surface area vs. time.
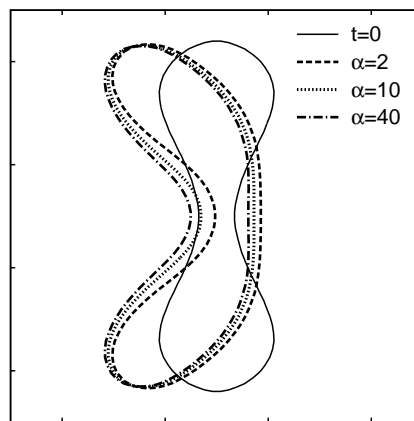

Figure 13: The comparison of the membrane shape for the surface dilation coefficient in x-z cross-section on $y = 0.25$.

The developments of the total surface area normalized by the initial surface area are compared in Fig. 12. As expected, the surface dilation is well maintained within the range of a few percent error, furthermore, it is effectively controlled by using larger α. The interfacial shapes at $t = 2$ in x-z cross-section are shown in Fig. 13. It is observed in a case of $\alpha = 40$, the surface deformation is most restricted.

3.4.2 Behavior of two capsules

Next, we consider two biconcave capsules with displacing the initial vertical positions. We prescribe two cases for different initial positions as;

$$\text{case 1:} \quad (x_c^{(1)}, y_c^{(1)}, z_c^{(1)}) = (0.125, 0.25, 0.25), \quad (x_c^{(2)}, y_c^{(2)}, z_c^{(2)}) = (0.375, 0.25, 0.25), \quad (3.8)$$

$$\text{case 2:} \quad (x_c^{(1)}, y_c^{(1)}, z_c^{(1)}) = (0.125, 0.25, 0.23), \quad (x_c^{(2)}, y_c^{(2)}, z_c^{(2)}) = (0.375, 0.25, 0.27). \quad (3.9)$$
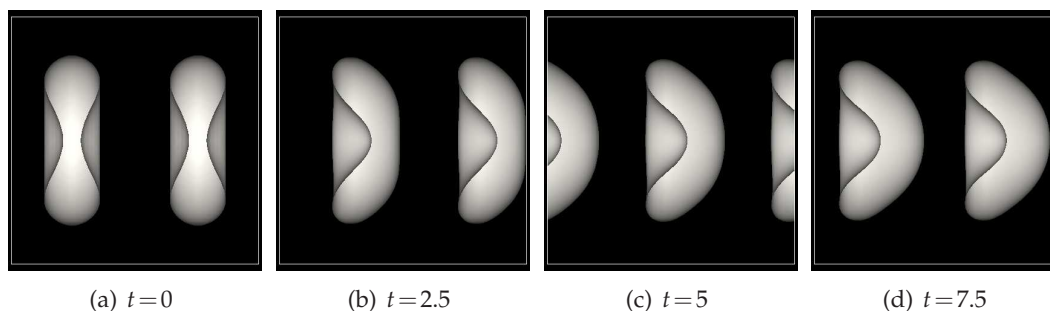
(a) $t=0$ (b) $t=2.5$ (c) $t=5$ (d) $t=7.5$

Figure 14: Evolution of the biconcave capsules in a pressure-driven flow. The initial location is of case 1 (3.8).

(a) $t=0$ (b) $t=2.5$ (c) $t=5$ (d) $t=7.5$
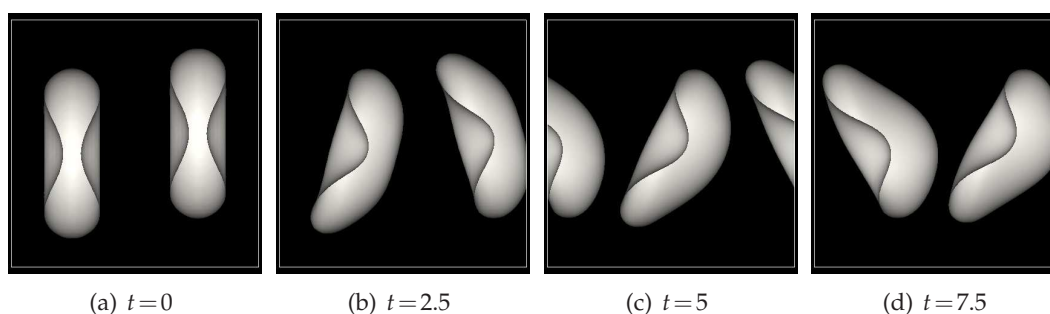
Figure 15: Same as Fig. 14, but the initial location is of case 2 (3.9).

The computational conditions are the same as Section 3.4.1, and we choose a restriction magnitude $\alpha=40$ from above investigation.

Sequential snapshots of the motion and deformation of the capsules are shown in Figs. 14 and 15. In case 1, two biconcave capsules are driven and symmetrically deforms, on the other hand in case 2, they deform with a rotation. In steady state, both results become a parabolic shape, so-called parachute-type shape which is well-known as one of the behaviors of a real RBC in a capillary tube [17]. Present solutions are quite similar to the results obtained by the immersed boundary method involving the Skalak model [19]. The interfacial shapes in x-z cross-section on $y=0.25$ are shown in Fig. 16. Interestingly, the initial vertical locations are different, nevertheless, the fluid area or gap between a membrane edge and wall boundary looks similar. To further validate our solution, the streamwisely-averaged velocity is plotted in Fig. 17, where a solution without capsules is also plotted. We confirm the flow is disturbed by the capsules, and the velocity profiles are slightly, but certainly, different in each case. This slight gap comes from a condition of the capsules at steady state, and it strongly depends on the initial location. About the sensitivity of the initial location, it was investigated in detail in [48].

3.4.3 Flow including multiple capsules

As a final test, we demonstrate the simulation for the pressure-driven flow including multiple biconcave capsules. The computational domain is the same as the above prob-
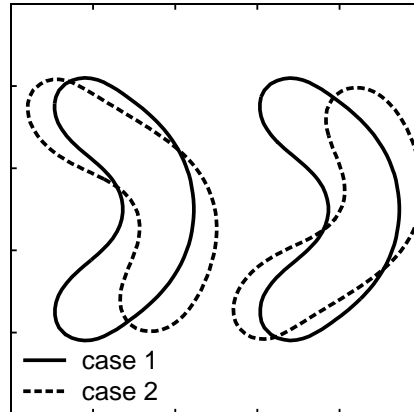
Figure 16: The interfacial shapes at $t=7.5$ with the initial location of case 1 and that of case 2, respectively.
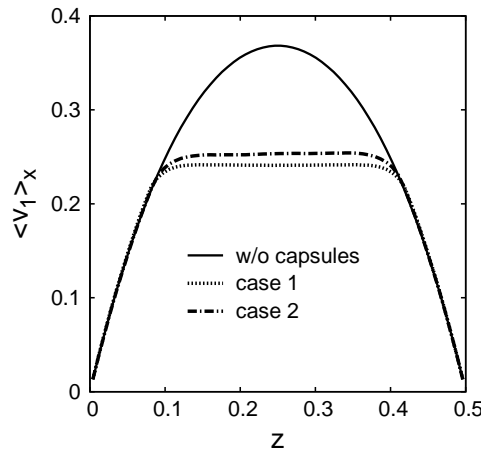

Figure 17: The velocity profile averaged for the streamwise direction x on $y=0.25$. The solutions are plotted at $t=7.5$ for the flows without capsules and with biconcave capsules on the initial locations of case 1 and case 2.

lem, but a refined mesh of $N^3=128^3$ is used. The material constants are set to $\rho_1=\rho_2=1$, $\mu_1=0.5$, $\mu_2=0.1$, $E_s=0.1$, $\alpha=10$, $E_b=5\times10^{-6}$ and $\Delta P/L=1$. Here, we use the equivalent radius of the biconcave capsule $a=0.06$ and the time increment $\Delta t=0.00025$. In this computation, the periodic boundary condition is imposed on both x and y directions for the computational efficiency. The numerical results are shown in Fig. 18. The capsules exhibit a complex pattern of motion and deformation due to interactions among themselves and with the surrounding fluid, especially near the wall at $t=4$ and $t=5$.

4   Conclusions

We have presented a full Eulerian fluid-membrane coupling method within the framework of the volume-of-fluid approach on the Cartesian coordinate mesh. The approx-
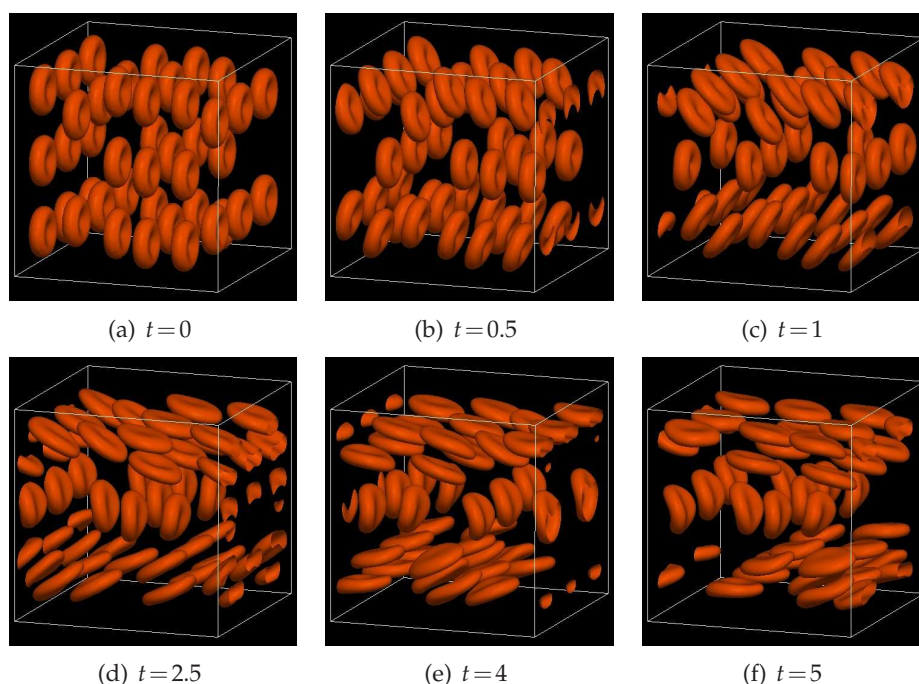
(a) $t=0$ (b) $t=0.5$ (c) $t=1$

(d) $t=2.5$ (e) $t=4$ (f) $t=5$

Figure 18: The instantaneous solutions for the multiple RBCs driven by a pressure gradient

.

imate delta function obtained from the smoothed VOF function enables us to involve the surface singular force coming from the membrane stress on the Eulerian mesh. Furthermore, the membrane in-plane stress is directly evaluated by introducing a part of the surface left Cauchy-Green deformation tensor as a prognostic variable defined on the Eulerian mesh, and it is updated on a compactly supported region or smoothed interfacial region. From the numerical point of view, the continuous interface capturing method was introduced for the advection of the smoothed VOF function, and it was extended with the convolution technique for the advection of the reference mean curvature to suppress the numerical dissipation and oscillation. In addition, we applied the quasi-implicit approach for the membrane in-plane stress, which improved the stability of the method without the need to solve a nonlinear system. Numerical results obtained by using the present full Eulerian approach show that our method is of the first-order accuracy. Our numerical results were compared with the ones using the (semi-Lagrangian) immersed boundary and (Lagrangian) boundary integral methods and good agreement has been obtained. Moreover, in the Skalak model, we confirmed the surface dilation of a membrane is controllable with a dilation coefficient, and a similar behavior of a red blood cell in a flow was observed.

One of the advantages of the present method compared with the traditional immersed boundary method [40,41] with the Lagrangian material points (or meshes) is to avoid the

instability occurred from the mesh distortion with large deformation. Another advantage of the present method is that the mass is strictly conservation, and the constructing of the color function which treats the different density and viscosity is not necessary because the interface is described by the smoothed VOF function, compared with the traditional front tracking method [18,51,52] in which the color function is calculated by solving the Poisson equation constructed from the information of the material points. Moreover, the full Eulerian approach can be easily parallelized with domain decomposition techniques that are often used in fluid flow simulations. Therefore, we believe that the present method has the novelty and effectiveness even with an $\mathcal{O}(\Delta x^1)$ accuracy.

The essential loss of accuracy comes from the coupling of the interfacial force and the numerical diffusion of the field variables on Eulerian meshes. Therefore, an implementation of a high order coupling techniques such as the immersed interface method [30,31,33] should help, which will be a future research subject. We would also apply the present method for a practical blood flow analysis including multiple red blood cells.

Acknowledgments

A Derivations of (2.16) and (2.17)

Take notice the definition of the surface gradient $\nabla_s = (\mathbf{I}-\mathbf{nn})\cdot\nabla = \mathbf{P}\cdot\nabla$, (2.16) changes into

$$
\begin{aligned}
\delta\nabla_s\cdot(\boldsymbol{\tau}+\mathbf{qn}) &= \delta P_{ik}\frac{\partial}{\partial x_k}(\tau_{ij}+q_i n_j) \\
&= P_{ik}\frac{\partial}{\partial x_k}(\delta(\tau_{ij}+q_i n_j)) - P_{ik}\frac{\partial\delta}{\partial x_k}(\tau_{ij}+q_i n_j) \\
&= \frac{\partial}{\partial x_k}(\delta P_{ik}(\tau_{ij}+q_i n_j)) - \frac{\partial P_{ik}}{\partial x_k}(\delta(\tau_{ij}+q_i n_j)) \\
&= \frac{\partial}{\partial x_k}(\delta P_{ik}(\tau_{ij}+q_i n_j)) - \frac{\partial(n_i n_k)}{\partial x_k}(\delta(\tau_{ij}+q_i n_j)) \\
&= \frac{\partial}{\partial x_k}(\delta(\tau_{kj}+q_k n_j)) \\
&= \nabla\cdot(\delta\boldsymbol{\tau}+\tilde{\mathbf{q}}\mathbf{n}),
\end{aligned}
\tag{A.1}
$$

where we use the following relationships,

$$\nabla_s \delta = 0, \quad \mathbf{n} \cdot \nabla \mathbf{n} = \mathbf{0}, \tag{A.2}$$

$$\mathbf{P} \cdot \boldsymbol{\tau} = \boldsymbol{\tau}, \quad \mathbf{n} \cdot \boldsymbol{\tau} = \mathbf{0}, \quad \mathbf{n} \cdot \mathbf{q} = 0, \tag{A.3}$$

from the definitions (2.4) and (2.7). In (A.1), $\tilde{\mathbf{q}}$ is defined as

$$
\begin{aligned}
\tilde{\mathbf{q}} = \delta \mathbf{q} &= \delta((\mathbf{P} \cdot \nabla) \cdot \mathbf{m}) \cdot \mathbf{P} = \delta P_{ik} \frac{\partial m_{il}}{\partial x_k} P_{lj} \\
&= P_{ik} \frac{\partial \delta m_{il}}{\partial x_k} P_{lj} - P_{ik} \frac{\partial \delta}{\partial x_k} m_{il} P_{lj} \\
&= \frac{\partial \delta P_{ik} m_{il}}{\partial x_k} P_{lj} - \frac{\partial P_{ik}}{\partial x_k} \delta m_{il} P_{lj} \\
&= \frac{\partial \delta m_{kl}}{\partial x_k} P_{lj} = (\nabla \cdot \tilde{\mathbf{m}}) \cdot \mathbf{P},
\end{aligned}
\tag{A.4}
$$

where we also use the relationships (A.2) and the definition (2.8). Finally, $\tilde{\mathbf{m}}$ is given as

$$\tilde{\mathbf{m}} = \delta \mathbf{m} = E_b(\delta \boldsymbol{\kappa} - \delta \kappa_R \mathbf{P}) = E_b(\delta \boldsymbol{\kappa} - \tilde{\kappa}_R \mathbf{P}). \tag{A.5}$$

B   Jacobian tensor in the present implicit approach

For the sake of simplicity in describing a tensor product involving the fourth-order one, the independent components of a symmetric second-order tensor $\mathbf{A}$ are written in a vector form such as $\mathbf{A}' = A'_i = (A_{11}, A_{22}, A_{33}, A_{12}, A_{23}, A_{31})$. Hereafter, a superscript $\prime$ indicates a vector consists of the independent components from a symmetric second-order tensor. Then, a second-order Jacobian tensor $\mathbf{J}'$ is given as

$$\mathbf{J}' = \frac{\partial \boldsymbol{\tau}'}{\partial \mathbf{B}'_s} \cdot \frac{\partial \mathbf{B}'_s}{\partial \mathbf{G}'_s}, \tag{B.1}$$

where $\partial \mathbf{B}'_s / \partial \mathbf{G}'_s$ is a second-order transform tensor. By using the definition $\mathbf{B}_s = \mathbf{P} \cdot \mathbf{G}_s \cdot \mathbf{P}$, a fourth-order transform tensor is given as

$$\frac{\partial B_{sij}}{\partial G_{skl}} = P_{ik} P_{lj}. \tag{B.2}$$

Taking notice of $B_{21} = B_{12}$, $B_{32} = B_{23}$ and $B_{13} = B_{31}$, (B.2) leads to a second-order transform tensor,

$$
\frac{\partial \mathbf{B}'_s}{\partial \mathbf{G}'_s} = \frac{\partial B'_{sj}}{\partial G'_{si}} =
\begin{bmatrix}
P_{11}P_{11} & P_{21}P_{12} & P_{31}P_{13} & 2P_{11}P_{12} & 2P_{21}P_{13} & 2P_{11}P_{13} \\
P_{12}P_{21} & P_{22}P_{22} & P_{32}P_{23} & 2P_{12}P_{22} & 2P_{22}P_{23} & 2P_{12}P_{23} \\
P_{13}P_{31} & P_{23}P_{32} & P_{33}P_{33} & 2P_{13}P_{32} & 2P_{23}P_{33} & 2P_{13}P_{33} \\
P_{11}P_{21} & P_{21}P_{22} & P_{31}P_{23} & P_{11}P_{22} & P_{21}P_{23} & P_{11}P_{23} \\
P_{12}P_{31} & P_{22}P_{32} & P_{32}P_{33} & P_{12}P_{32} & P_{22}P_{33} & P_{12}P_{33} \\
P_{11}P_{31} & P_{21}P_{32} & P_{31}P_{33} & P_{11}P_{32} & P_{21}P_{33} & P_{11}P_{33}
\end{bmatrix},
\tag{B.3}
$$

where $\mathbf{P} = \mathbf{I} - \mathbf{nn}$ is the second-order surface projection tensor.

Here from (2.4), the derivative of the in-plane stress is written as

$$\frac{\partial \boldsymbol{\tau}'}{\partial \mathbf{B}'_s} = \frac{2}{\sqrt{c_2}} \left(\frac{\partial W_{s,c_1}}{\partial c_1} \frac{\partial c_1}{\partial \mathbf{B}'_s} \mathbf{B}'_s + c_2 \frac{\partial W_{s,c_2}}{\partial c_2} \frac{\partial c_2}{\partial \mathbf{B}'_s} \mathbf{P}' + \frac{1}{2} \frac{\partial c_2}{\partial \mathbf{B}'_s} \left(-\frac{W_{s,c_1}}{c_2} \mathbf{B}'_s + W_{s,c_2} \mathbf{P}' \right) + W_{s,c_1} \mathbf{I} \right), \quad \text{(B.4)}$$

where

$$W_{s,c_1} = \frac{\partial W_s}{\partial c_1}, \quad W_{s,c_2} = \frac{\partial W_s}{\partial c_2}, \quad \text{(B.5)}$$

depends on a strain energy function of a membrane model, and we consider $\partial W_{s,c_1} / \partial c_2 = \partial W_{s,c_2} / \partial c_1 = 0$ for the specific model (2.5) or (2.6).

By using (B.3) and (B.4), the second-order Jacobian tensor (B.1) is obtained, and the second-order tensor $\mathbf{H}(\mathbf{v}, \mathbf{G}_s, \mathbf{J})$ in (2.34) is shown as

$$\mathbf{H}(\mathbf{v}, \mathbf{G}_s, \mathbf{J}) = \mathbf{J} : (\nabla \mathbf{v}^T \cdot \mathbf{G}_s + \mathbf{G}_s \cdot \nabla \mathbf{v}) = \begin{bmatrix} J'_{1j} R'_j & J'_{4j} R'_j & J'_{6j} R'_j \\ J'_{4j} R'_j & J'_{2j} R'_j & J'_{5j} R'_j \\ J'_{6j} R'_j & J'_{5j} R'_j & J'_{3j} R'_j \end{bmatrix}, \quad \text{(B.6)}$$

where $\mathbf{R}'$ is given by

$$\mathbf{R}' = \begin{bmatrix} 2\left(\frac{\partial v_1}{\partial x} G_{s11} + \frac{\partial v_1}{\partial y} G_{s12} + \frac{\partial v_1}{\partial z} G_{s31} \right) \\ 2\left(\frac{\partial v_2}{\partial x} G_{s12} + \frac{\partial v_2}{\partial y} G_{s22} + \frac{\partial v_2}{\partial z} G_{s23} \right) \\ 2\left(\frac{\partial v_3}{\partial x} G_{s31} + \frac{\partial v_3}{\partial y} G_{s23} + \frac{\partial v_3}{\partial z} G_{s33} \right) \\ \frac{\partial v_2}{\partial x} G_{s11} + \frac{\partial v_1}{\partial y} G_{s22} + \left(\frac{\partial v_1}{\partial x} + \frac{\partial v_2}{\partial y} \right) G_{s12} + \frac{\partial v_1}{\partial z} G_{s23} + \frac{\partial v_2}{\partial z} G_{s31} \\ \frac{\partial v_3}{\partial y} G_{s22} + \frac{\partial v_2}{\partial z} G_{s33} + \frac{\partial v_3}{\partial x} G_{s12} + \left(\frac{\partial v_2}{\partial y} + \frac{\partial v_3}{\partial z} \right) G_{s23} + \frac{\partial v_2}{\partial x} G_{s31} \\ \frac{\partial v_3}{\partial x} G_{s11} + \frac{\partial v_1}{\partial z} G_{s33} + \frac{\partial v_3}{\partial y} G_{s12} + \frac{\partial v_1}{\partial y} G_{s23} + \left(\frac{\partial v_1}{\partial x} + \frac{\partial v_3}{\partial z} \right) G_{s31} \end{bmatrix}, \quad \text{(B.7)}$$

from the definition of $\mathbf{R} = \nabla \mathbf{v}^T \cdot \mathbf{G}_s + \mathbf{G}_s \cdot \nabla \mathbf{v}$.

References

[1] D. Barthés-Biesel and J.M. Rallison, The time-dependent deformation of a capsule freely suspended in a linear shear flow, J. Fluid. Mech., 113 (1981) 251–267.

[2] T.J. Barth and P.O. Frederickson, High-Order Solution of the Euler Equations on Unstructured Grids Using Quadratic Reconstruction, AIAA Paper, 90-0013 (1990).

[3] J.U. Brackbill, D.B. Kothe, C. Zemach, A continuum method for modeling surface tension, J. Comput. Phys., 100 (1992) 335–354.

[4] D.J. Benson, Computational methods in Lagrangian and Eulerian hydrocodes, Comput. Methods Appl. Mech. Eng., 99(1992) 235–394.

[5] H.D. Ceniceros, J.E. Fisher, A.M. Roma, Efficient solutions to robust, semi-implicit discretizations of the immersed boundary method, J. Comput. Phys., 228 (2009) 7137–7158.

[6] G.H. Cottet and E. Maitre, A level set method for fluid-structure interactions with immersed surfaces, Math. Model. Meth. Appl. Sci., 16 (2006) 415–438.

[7] G.H. Cottet, E. Maitre, T. Milcent, Eulerian formulation and level set models for incompressible fluid-structure interaction, Math. Modeling and Numer. Anal., 42 (2008) 471–492.

[8] S.J. Cummins, M.M. Francois, D.B. Kothe, Estimating curvature from volume fractions, Comput. Structures, 83 (2005) 425–434.

[9] T. Dunne, An Eulerian approach to fluid-structure interaction and goal-oriented mesh adaptation, Int. J. Numer. Meth. Fluids, 51 (2006) 1017–1039.

[10] C.D. Eggleton and A.S. Popel, Large deformation of red blood cell ghosts in a simple shear flow, Phys. Fluids, 10 (1998) 2182–2189.

[11] E. Evans, Y. Fung, Improved measurement of the erythrocyte geometry, Microvasc Res., 4 (1972) 335–347.

[12] L. Fauci, C.S. Peskin, A computational model of aquatic animal locomotion, J. Comput. Phys., 77 (1988) 86–108.

[13] P.A. Ferdowsi, M. Bussmann, Second-order accurate normals from height functions, J. Comput. Phys., 227 (2008) 9293–9302.

[14] A.L. Fogelson, A mathematical model and numerical method for studying platelet adhesion and aggregation during blood clotting, J. Comput. Phys., 56 (1984) 111–134.

[15] A.L. Fogelson, Continuum models of platelet aggregation: formulation and mechanical properties, SIAM J. Appl. Math., 52 (1992) 1089–1110.

[16] M.M. Francois, S.J. Cummins, E.D. Dendy, D.B. Kothe, J.M. Sicilian, M.W. Williams, A balanced-force algorithm for continuous and sharp interfacial surface tension models within a volume tracking framework, J. Comput. Phys., 213 (2006) 141–173.

[17] P. Gaehtgens, C.Dührssen and K.H.Albrecht, Motion, deformation, and interaction of blood cells and plasma during flow through narrow capillary tubes. Blood Cells, 6 (1980) 799–817.

[18] J. Glimm, J.W. Grove, X.L. Li, K.M. Shyue, Y.N. Zeng and Q. Zhang, Three-dimensional front tracking, SIAM J. Sci. Comp., 19 (1998) 703–727.

[19] X. Gong, K. Sugiyama, S. Takagi, Y. Matsumoto, The deformation behavior of multiple red blood cells in a capillary vessel, J. Biomech. Eng., 131 (2009) 074504.

[20] F.H. Harlow, J.E. Welch, Numerical calculation of time-dependent viscous incompressible flow of fluid with free surface, Phys. Fluids, 8 (1965) 2182–2189.

[21] T.Y. Hou, Z. Shi, Removing the stiffness of elastic force from the immersed boundary method for 2D Stokes equations, J. Comput. Phys., 227 (2008) 9138–9169.

[22] T.Y. Hou, Z. Shi, An efficient semi-implicit immersed boundary method for the Navier-Stokes equations, J. Comput. Phys. 227 (2008) 8968–8991.

[23] C.W. Hirt, B.D. Nichols, Volume of fluid (VOF) method for the dynamics of free boundaries, J. Comput. Phys., 39 (1981) 201–225.

[24] S. Ii and F. Xiao, A simplified interface capturing scheme using a continuous function, Proc. of SNA+MC 2010, (2010).

[25] S. Ii, K. Sugiyama, S. Takeuchi, S. Takagi and Y. Matsumoto, An implicit full Eulerian method for the fluid-structure interaction problem, Int. J. Numer. Meth. Fluids, 65 (2011) 150–165.

[26] S. Ii, K. Sugiyama, S. Takeuchi, S. Takagi, Y. Matsumoto and F. Xiao, An interface capturing method with a continuous function: the THINC method with multi-dimensional reconstruction, J. Comput. Phys., 231 (2012) 2328–2358.

[27] G.S. Jiang, C.W. Shu, Efficient implementation of WENO schemes, J. Comput. Phys., 126 (1996) 202–228.

[28] T. Kajishima, Conservation properties of finite difference method for convection, Trans. Jpn.

Soc. Mech. Eng. B, 60 (1994) 2058–2063 (in Japanese).

[29] M.C. Lai and C.S. Peskin, An Immersed Boundary Method with Formal Second-Order Accuracy and Reduced Numerical Viscosity, J. Comput. Phys., 160 (2000) 705–719.

[30] R.J. LeVeque, Z. Li, The immersed interface method for elliptic equations with discontinuous coefficients and singular sources, SIAM J. Numerical Analysis, 31 (1994) 1019–1044.

[31] D.V. Le, B.C. Khoo, J. Peraire, An immersed interface method for viscous incompressible flows involving rigid and flexible boundaries, J. Comput. Phys., 220 (2006) 109–138.

[32] D.V. Le, J. White, J. Peraire, K.M. Lim and B.C. Khoo, An implicit immersed boundary method for three-dimensional fluid-membrane interactions, J. Comput. Phys., 228 (2009) 8427–8445.

[33] Z. Li, M.C. Lai, The immersed interface method for the Navier-Stokes equations with singular forces, J. Comput. Phys., 171 (2001) 822–842.

[34] C. Liu, N.J. Walkington, An Eulerian description of fluids containing visco-elastic particles, Arch. Rational Mech. Anal., 159 (2001) 229–252.

[35] J. López, J. Hernández, On reducing interface curvature computation errors in the height function technique, J. Comput. Phys., 229 (2010) 4855–4868.

[36] Y. Mori, C.S. Peskin, Implicit second-order immersed boundary methods with boundary mass, Comput. Methods Appl. Mech. Eng., 197 (2008) 2049–2067.

[37] N. Nagano, K. Sugiyama, S. Takeuchi, S. Ii, S. Takagi and Y. Matsumoto, Full-Eulerian Finite-Difference Simulation of Fluid Flow in Hyperelastic Wavy Channel, Journal of Fluid Science and Technology, 5 (2010) 475–490.

[38] S. Okazawa, K. Kashiyama, Y. Kaneko, Eulerian formulation using stabilized finite element method for large deformation solid dynamics, Int. J. Numer. Meth. in Engng., 72 (2007) 1544–1559.

[39] S.J. Osher, J.A. Sethian, Fronts propagating with curvature dependent speed. Algorithms based on Hamilton-Jacobi formulations, J. Comput. Phys., 79 (1988) 12–49.

[40] C.S. Peskin, Flow patterns around heart valves: a numerical method, J. Comput. Phys., 10 (1972) 252–271.

[41] C.S. Peskin, The immersed boundary method, Acta Numerica, 11 (2002) 479–517.

[42] J.E. Pilliod Jr., E.G. Puckett, Second-order accurate volume-of-fluid algorithms for tracking material interfaces, J. Comput. Phys., 199 (2004) 465–502.

[43] C. Pozrikidis, Finite deformation of liquid capsules enclosed by elastic membranes in simple shear flow, J. Fluid. Mech., 297 (1995) 123–152.

[44] C. Pozrikidis, Effect of bending stiffness on the deformation of liquid capsules in simple shear flow, J. Fluid. Mech., 440 (2001) 269–291.

[45] R. Skalak, A. Tözeren, P.R. Zarda and S. Chien, Strain energy function of red blood cell membranes, Biophys. J., 13 (1973) 245–264.

[46] P.A. Stewart, N.Lay, M.Sussman and M. Ohta, An Improved Sharp Interface Method for Viscoelastic and Viscous Two-Phase Flows, J. Sci. Comp., 35 (2008) 43–61.

[47] M. Sussman, P. Smereka, S. Osher, A level set approach for computing solutions to incompressible two-phase flows, J. Comput. Phys., 114 (1994) 146–159.

[48] K. Sugiyama, S. Ii, S. Takeuchi, S. Takagi and Y. Matsumoto, Full Eulerian simulations of biconcave neo-Hookean particles in a Poiseuille flow, Comput. Mech., 46 (2010) 147–157.

[49] K. Sugiyama, S. Ii, S. Takeuchi, S. Takagi, Y. Matsumoto, A full Eulerian finite difference approach for solving fluid-structure coupling problems, J. Comput. Phys., 230 (2011) 596–627.

[50] G.I. Taylor, The deformation of emulsions in definable fields of flows, Proc. R. Soc. Lond. A,

146 (1934) 501–523.

[51] G. Tryggvason, B.B. Bunner, A. Esmaeeli, D. Juric, N. Al-Rawahi, W. Tauber, J. Han, S. Nas, Y.J. Jan, A front-tracking method for the computations of multiphase flow, J. Comput. Phys., 169 (2001) 708–759.

[52] S.O. Unverdi, G. Tryggvason, A front-tracking method for viscous, incompressible, multi-fluid flows, J. Comput. Phys., 100 (1992) 25–37.

[53] P.A.A Van Hoogstraten, P.M.A Slaats, F.P.T. Baaijens, A Eulerian approach to the finite element modeling of neo-Hookean rubber material, Appl. Sci. Res., 48 (1991) 193–210.

[54] F. Xiao, T. Yabe, Computation of complex flows containing rheological bodies, Computational Fluid Dynamics J., 8 (1999) 43–49.

[55] F. Xiao, Y. Honma, K. Kono, A simple algebraic interface capturing scheme using hyperbolic tangent function, Int. J. Numer. Meth. Fluids, 48 (2005) 1023–1040.

[56] K. Yokoi, Efficient implementation of THINC scheme: A simple and practical smoothed VOF algorithm, J. Comput. Phys., 226 (2007) 1985–2002.

[57] D.L. Youngs, Time-dependent multi-material flow with large fluid distortion, in K.W. Morton and M.J. Baines (eds), Numerical Methods for Fluid Dynamics, Academic, New York, 1982, 273–285.

[58] D.L. Youngs, An Interface Tracking Method for a 3D Eulerian Hydrodynamics Code, Technical Report, 44/92/35, AWRE, 1984.